Characterization of organic aerosol across the global remote troposphere: A comparison of ATom measurements and global chemistry models

Alma Hodzic[1], Pedro Campuzano-Jost[2,3], Huisheng Bian[4], Mian Chin[4], Peter R. Colarco[4], Douglas A. Day[2,3], Karl D. Froyd[2,8], Bernd Heinold[6], Duseong S. Jo[2,3], Joseph M. Katich[2,8], John K. Kodros[5], Benjamin A. Nault[2,3], Jeffrey R. Pierce[5], Eric Ray[2,8], Jacob Schacht[6], Gregory P. Schill[2,8], Jason C. Schroder[2,3], Joshua P. Schwarz[2,8], Donna T. Sueper[2,3], Ina Tegen[6], Simone Tilmes[1], Kostas Tsigaridis[7,9], Pengfei Yu[8,10], Jose L. Jimenez[2,3]

[1]National Center for Atmospheric Research, Boulder, CO, USA

[2]Cooperative Institute for Research in Environmental Sciences (CIRES), University of Colorado, Boulder, CO, USA

[3]Department of Chemistry, University of Colorado, Boulder, CO, USA

[4]NASA Goddard Space Flight Center, Greenbelt, MD, USA

[5]Department of Atmospheric Science, Colorado State University, Fort Collins, CO, USA

[6]Leibniz Institute for Tropospheric Research, Leipzig, Germany

[7]Center for Climate Systems Research, Columbia University, New York, NY, USA

[8]NOAA Earth System Research Laboratory (ESRL), Chemical Sciences Division, Boulder, CO, USA

[9]NASA Goddard Institute for Space Studies, New York, NY, USA

[10]Institute for Environmental and Climate Research, Jinan University, Guangzhou, Guangdong, China

Key words: organic aerosol, remote atmosphere, ATom field campaign.

Abstract.

The spatial distribution and properties of submicron organic aerosols (OA) are among the key sources of uncertainty in our understanding of aerosol effects on climate. Uncertainties are particularly large over remote regions of the free troposphere and Southern Ocean, where very little data has been available, and where OA predictions from AeroCom Phase II global models span two to three orders-of-magnitude, greatly exceeding the model spread over source regions. The (nearly) pole-to-pole vertical distribution of non-refractory aerosols was measured with an aerosol mass spectrometer onboard the NASA DC8 aircraft as part of the Atmospheric Tomography (ATom) mission during the northern hemisphere summer (August 2016) and winter (February 2017). This study presents the first extensive characterization of OA mass concentrations and their level of oxidation in the remote atmosphere. OA and sulfate are the major contributors by mass to submicron aerosols in the remote troposphere, together with sea salt in the marine boundary layer. Sulfate was dominant in the lower stratosphere. OA concentrations have a strong seasonal and zonal variability, with the highest levels measured in the lower troposphere in the summer and over the regions influenced by the biomass burning from Africa (up to 10 $\mu g\ sm^{-3}$). Lower concentrations (~0.1-0.3 $\mu g\ sm^{-3}$) are observed in the northern mid- and high- latitudes and very low concentrations (< 0.1 $\mu g\ sm^{-3}$) in the southern mid- and high- latitudes. The ATom dataset is used to evaluate predictions of eight current global chemistry models that implement a variety of commonly used representations of OA sources and chemistry, as well as of the AeroCom-II ensemble. The current model ensemble captures the average vertical and spatial distribution of measured OA concentrations, and the spread of the individual models remains within a factor of 5. These results are significantly improved over the AeroCom-II model ensemble, which shows large overestimations over these regions. However, some of the improved agreement with observations occurs for the wrong reasons, as models have the tendency to greatly overestimate the primary OA fraction, and underestimate the secondary fraction. Measured OA in the remote free troposphere are highly oxygenated with organic aerosol to organic carbon (OA/OC) ratios of ~ 2.2-2.8 and are 30-60% more oxygenated than in current models, which can lead to significant errors in OA concentrations. The model/measurement comparisons presented here support the concept of a more dynamic OA system as proposed by Hodzic et al. (2016), with enhanced removal of primary OA, and a stronger production of secondary OA in global models needed to provide a better agreement with observations.

1 Introduction

Organic aerosols (OA) are a complex mixture of directly emitted primary OA (POA) and chemically produced secondary OA (SOA) from anthropogenic and biogenic emission sources. They are associated with adverse health effects (Mauderly and Chow, 2008, Shiraiwa et al., 2017) and contribute radiative forcing in the climate system (Boucher et al., 2013). The currently limited understanding of processes involved in the formation, ageing, and removal of organic compounds results in large uncertainties in (i) the predicted global OA burden, (ii) relative contributions of emissions vs. chemistry to OA formation, (iii) spatial distribution, and (iv) impacts on radiation and clouds (Kanakidou et al., 2005, Hallquist et al., 2009, Heald et al., 2011, Spracklen et al., 2011, Tsigaridis et al., 2014, Hodzic et al., 2016, Shrivastava et al., 2017, Tsigaridis and Kanakidou, 2018, Zhu et al., 2019). The uncertainties are particularly large in the estimated global burden of SOA that range from 12 to 450 Tg y^{-1} (see Fig. 9 of Hodzic et al., 2016), and in their direct and indirect radiative forcing that range from -0.08 to -0.33 W m^{-2}, and -0.60 to −0.77 W m^{-2}, respectively (Spracklen et al., 2011, Myhre et al., 2013, Scott et al., 2014, Hodzic et al., 2016, Tsigaridis and Kanakidou, 2018). Reducing these uncertainties is becoming more important as OA is on a path to becoming the dominant fraction of the submicron anthropogenic aerosol mass globally due to the ongoing efforts to reduce SO_2 emissions and associated sulfate aerosols.

Model performance has been especially poor in the remote regions of the atmosphere where OA measurements available for model evaluation have been sparse (especially aloft). Using data from 17 aircraft campaigns mostly located in the northern hemisphere Heald et al. (2011) showed that the skill of the global GEOS-Chem model in predicting the vertical distribution of OA was significantly decreased in remote regions compared to polluted near-source regions. The study pointed out the limitations of commonly used SOA formation mechanisms that are based on chamber data; these have the tendency to underpredict OA in source regions and overpredict OA in the remote troposphere. For a subset of 9 recent aircraft campaigns, Hodzic et al. (2016) showed that OA is likely a more dynamic system than represented in chemistry-climate models, with both stronger production and stronger removals. These authors suggested that additional removal mechanisms via e.g. photolytic or heterogeneous reactions of OA particles are needed to explain low OA concentrations observed in the upper troposphere where direct cloud scavenging is less efficient. The recent global multi-model comparison study (Tsigaridis

et al., 2014) within the AeroCom Phase II project illustrates well the amplitude of model uncertainties simulating OA mass concentrations and the contrast in model performance between near-source and remote regions. The results indicate that model dispersion (the spread between the models with the lowest and highest predicted OA concentrations) increases with altitude from roughly 1 order of magnitude near the surface to 2-3 orders of magnitude in the upper troposphere. Our own analyses of the AeroCom-II models shown in Figure 1a indicate that model dispersion (quantified as the ratio of the average concentration of the highest model to that of the lowest one, in each region) increases not only with altitude but also with distance from the northern mid-latitude source (and data-rich) regions. The model spread is a factor of 10-20 in the free troposphere between the equator and northern mid-latitudes, and increases to a factor of 200-800 over the Southern Ocean and near the tropopause. It is not surprising that model spread is lower closer to source regions where it is mostly driven by uncertainties in emissions and SOA production yields. Spread is expected to be larger in remote regions where models are also impacted by uncertainties in transport, chemical ageing and removal. The lowest model dispersion also coincides with the regions of the northern hemisphere (NH) or the African biomass burning outflow where models have been evaluated the most (Figure 1b), emphasizing the need for further model/observation comparison studies in remote regions (of the southern hemisphere (SH) in particular).

Here, we present a unique data set of airborne aerosol mass spectrometer measurements of OA mass concentrations collected onboard the NASA DC-8 as part of the Atmospheric Tomography (ATom) mission. The aircraft sampled the vertical structure of the atmosphere from near-surface (0.2 km) to the lower-stratosphere (LS) regions (12 km altitude) over both the Pacific and Atlantic basins (to limit the influence of source regions) with a quasi-global spatial coverage from 82°N to 67°S. This dataset is used to perform the first systematic global-scale multi-model evaluation of the chemistry-climate models focusing on OA in the remote troposphere over the remote oceans. We focus on the NH summer (August 2016, ATom-1) and NH winter (February 2017, ATom-2) deployments. Overall these ATom missions sampled the marine boundary layer (MBL) for 10% of the flight tracks, 12% of the time the remote lower stratosphere, and the rest the free troposphere. The model-observation comparisons are aimed at identifying discrepancies in terms of OA mass concentrations and vertical distribution, their fractional contribution to submicron aerosols, and their oxidation level in global models.

The modeling framework is described in Section 2. Section 3 describes the ATom dataset and the spatial and vertical distributions of OA over the Atlantic and Pacific regions. Section 4 presents the comparisons of ATom-1 and -2 data to multi-model predictions from both the AeroCom-II models, and the ensemble of eight current model simulations of the ATom campaign. Section 5 presents the conclusions of the study and discusses its implications.

2 Modeling framework

2.1 ATom model simulations

ATom measurements were compared with results of eight global models that simulated the time period of the ATom-1 and 2 campaigns (August 2016 and February 2017), using the emissions and reanalysis meteorology corresponding to this period (and a spin-up time of at least six to twelve months). These are referred hereafter as ATom models and include the NASA global Earth system model GEOS5, the aerosol-climate model ECHAM6-HAM, three versions of the NCAR Community Earth System Model (CESM), and three versions of the global chemistry GEOS-Chem model. Simulations were performed at various horizontal resolutions ranging from relatively high ~50km (GEOS5) and ~100km (CESM2 models) resolutions to somewhat coarser grids of ~200km (CESM1-CARMA, GEOS-Chem) and ~400km for GC10-TOMAS. The advantage of using the same host model (in the cases of variants of CESM2 and GEOS-Chem) is that the dynamics and emissions remain comparable. Models differ greatly in their treatment of emissions, gas-phase chemistry, aerosol chemistry and physical processes, and aerosol coupling with radiation and clouds, among others. Table 1 describes the configuration of various models (e.g. meteorology, emissions), and their treatment of OA. In this section we only summarize the main features and parameters directly impacting the OA simulations. Some models do not include SOA chemistry and instead assume that SOA is directly emitted proportional to the emissions of its precursors (ECHAM6-HAM, CESM2-SMP, GEOS5, GC10-TOMAS), while others have more complex treatments of organic compounds, their chemistry, and partitioning into particles (GC12-REF, GC12-DYN, GC10-TOMAS, CESM1-CARMA, CESM2-DYN). It should be noted that models that directly emit SOA assume that SOA is a non-volatile species that remains irreversibly in the particle phase. In all models POA is treated as a non-volatile directly emitted species. In most models (see below) the primary emitted organic aerosol is artificially aged to transition between hydrophobic to hydrophilic POA. There are some commonalities between simulations for

the treatment of biogenic emissions, which are based in all models on the Model of Emissions of Gases and Aerosols from Nature (MEGAN, Guenther et al., 2012) to generate meteorology-dependent emissions of volatile organic compounds. None of the models includes the marine production of OA which is estimated to be ~3 orders of magnitude smaller than the continental production of OA from both isoprene and monoterpene precursors (Kim et al., 2017), but could be important in the MBL. This contribution could however be larger for sea-spray biological material from phytoplankton with predicted contributions of 0.01 to 0.1 $\mu g\ m^{-3}$ to surface submicron aerosol over remote oceanic regions (Vergara-Temprado et al., 2017, Middlebrook et al., 1998). Below we only provide a brief description of most important processes that influence OA for each model.

GEOS5 was run in a configuration similar to Bian et al. (2019) using the anthropogenic emissions from HTAP v2 (Janssens-Maenhout et al., 2015) and biomass burning emissions from the Quick Fire Emission Dataset (QFED v2.54). Aerosols are simulated within the GOCART bulk aerosol module and include externally mixed particles of black carbon (BC), organic carbon (OC), sulfate, ammonium, nitrate, dust and sea salt (Colarco et al., 2010, Bian et al., 2017). The formation of SOA is based on a prescribed 10% formation yield from the monoterpene emissions. The primary emitted OC and SOA are separated into hydrophobic (50%) and hydrophilic (50%) species, with a 2.5 days e-folding time conversion from hydrophobic to hydrophilic organic particles. All SOAs from biogenic, anthropogenic, and biomass burning sources are treated as hydrophilic particles. Both types of organic particles are dry deposited. The hydrophilic OA is removed by large-scale and convective warm clouds, while hydrophobic OA is removed by ice clouds. The hydrophilic particles undergo hygroscopic growth according to the equilibrium parameterization of Gerber (1985).

The ECHAM6.3-HAM2.3 standard version (Tegen et al., 2019) was run using updated anthropogenic emissions (Schacht et al, 2019) combining the ECLIPSE (Klimont et al., 2017) emissions, with the Russian anthropogenic BC emissions from Huang et al. (2015). For biomass burning the Global Fire Assimilation System (GFAS, Kaiser et al., 2012) biomass burning emissions are used, however, without the scaling factor of 3.4 suggested by Kaiser et al. (2012). Aerosol composition and processes are simulated using the Hamburg Aerosol Model (HAM2, Zhang et al., 2012), that considers an aerosol internal mixture of sulfate, BC, OC, sea salt, and mineral dust. The aerosol population and their microphysical interactions are simulated using seven log-normal modes, including the

nucleation mode, soluble and insoluble Aitken, accumulation and coarse modes. In the model configuration used in this publication the formation of SOA is based on a prescribed 15% mass yield from monoterpene emissions only (Dentener et al., 2006). Aerosol particles are removed by dry and wet deposition. The wet deposition includes the below cloud scavenging by rain and in-cloud cloud scavenging for large-scale and convective systems (Croft et al., 2010).

The two simulations with the GEOS-Chem 12.0.1 global chemistry model (Bey et al., 2001) use emissions based on CMIP6 global inventory (CEDS historical emissions up to 2014 and future emissions based on climate scenarios, Hoesly et al., 2018; Feng et al., 2019) with regional improvements for anthropogenic sources, and on GFED v.4 for biomass burning emissions (Giglio et al., 2013). Both simulations use the bulk aerosol representation and differ only in the treatment of SOA formation and removal. The first configuration (called hereafter GC12-REF) includes the default (http://wiki.seas.harvard.edu/geos-chem/index.php) representation of SOA formation based on Marais et al. (2016) for isoprene-derived SOA, and on the volatility basis set (VBS) of Pye et al. (2010) for all other precursors. Note that this GEOS-Chem REF simulation is similar to the version 12 default “complex option” which includes non-volatile POA and semi-volatile SOA (semi-volatile POA is an optional switch within this version used in Pai et al. 2020). The second configuration (referred to as GC12-DYN) includes a more dynamic representation of the SOA lifecycle based on Hodzic et al. (2016), with the exception of the treatment of isoprene SOA that is formed in the aqueous aerosols as in Marais et al. (2016). As in Hodzic et al. (2016) the GC12-DYN model version includes updated VBS SOA parameterization, updated dry and wet removal of organic vapors, and photolytic removal of SOA (except for isoprene-SOA). SOA formation is based on wall-corrected chamber yields (Zhang et al., 2014) for the traditional precursors (isoprene, monoterpenes, sesquiterpenes, benzene, toluene, xylene) and on yields derived from an explicit chemical mechanism for higher molecular weight n-alkanes and n-alkenes species (Hodzic et al., 2016). The removal of gas-phase oxidized volatile organics uses updated Henry’s law solubility coefficients from Hodzic et al. (2014), and photolytic removal of SOA (Hodzic et al., 2015). In addition to OA, the model includes BC and dust, and simulates the chemistry and gas-particle partitioning of inorganic compounds such as sulfate, ammonium, nitrate and sea salt using the ISORROPIA II thermodynamic model (Fountoukis and Nenes, 2007). In both GEOS-Chem configurations, BC and primary OC are simulated with a hydrophobic and hydrophilic fraction for each. At the time of emission,

80% of BC and 50% of primary OC are considered as hydrophobic. Hydrophobic aerosols are converted to hydrophilic aerosols with an e-folding lifetime of 1.15 days. An OA/OC ratio of 2.1 is assumed to convert POC to POA, and SOA is simulated as OA mass (i.e. no OA/OC ratio assumption is needed for SOA, except for comparison with OC measurements). Soluble gases and aerosols are removed by both dry and wet deposition. Wet deposition includes scavenging in convective updrafts, and in-cloud and below-cloud scavenging from large-scale precipitation (Liu et al., 2001). Hydrophobic aerosols (BC and POA) are scavenged in convective updrafts following Wang et al. (2014).

GC10-TOMAS is based on the GEOS-Chem version 10.01 coupled with TwO Moment Aerosol Sectional microphysics scheme (TOMAS) and ran in a similar configuration to that described in Kodros et al. (2016). The model computes the evolution of sulfate, sea salt, primary and secondary OA, BC, and dust aerosols described by 15 internally mixed size bins (of which six were analyzed for these comparisons, cf. Table 1). Anthropogenic emissions are based on the EDGAR v4 global inventory with regional improvements, while the biomass burning emissions are from GFED v3. SOA are irreversibly made from the emitted parent precursor, considering a 10% mass yield from monoterpene emissions, and an emission flux of 0.2 Tg of SOA per Tg of CO for the anthropogenic CO emissions. The removal of gases and aerosols are treated similar to the GEOS-Chem 12.0.1 model (GC12-REF, see above).

Simulations based on the CESM2.0 Earth system model use the standard version of the Whole Atmosphere Community Climate Model (WACCM6, Gettelman et al., 2019, Emmons et al., 2019). Details on the specific of the model configurations are described in detail in Tilmes et al. (2019) i.e. CESM2-SMP and CESM2-DYN correspond to the specified dynamics WACCM6-SOAG and WACCM6-VBSext simulations described in that work, respectively. Emissions are based on the CMIP6 global inventory for the year 2014 for anthropogenic sources, and on the QFED version 2.4 for the wildfires inventory. Aerosols are represented with the modal aerosol scheme (MAM4, Liu et al., 2012) that includes BC, primary and secondary OA, sulfate, dust and sea salt. Four modes are considered including Aitken, accumulation and coarse size modes, and an additional primary carbon mode. Only the accumulation mode was used in this work. The CESM2-SMP and CESM2-DYN simulations differ in their treatment of OA. CESM2-SMP forms OA directly using fixed mass yields from primary emitted precursors (isoprene, monoterpenes, aromatics) without explicitly simulating their oxidation and partitioning. These mass yields

are increased by a factor of 1.5 to match the anthropogenic aerosol indirect forcing (Liu et al., 2012). The second configuration (referred to as CESM2-DYN) includes the formation and removal parameterizations of organics of Hodzic et al. (2016), as implemented into CESM2 by Tilmes et al. (2019) for all species based on low-NOx VBS yields only. This is a similar SOA scheme as used in GC12-DYN (with differences in the treatment of isoprene-SOA based on Marais et al. 2016 in GC12-DYN, and the use of both low- and high-NOx VBS yields in GC12-DYN). Organic gases and aerosols undergo dry and wet deposition as described in Liu et al. (2012). It should be noted that CESM2-SMP does not include deposition of intermediate organic vapors. Aerosol wet scavenging considers in-cloud scavenging (the removal of cloud-borne particles that were activated at the cloud base) and below-cloud scavenging for both convective and grid-scale clouds.

CESM1-CARMA simulations use the configuration described in Yu et al. (2019) which is based on CESM1 and the sectional Community Aerosol and Radiation Model for Atmospheres (CARMA v3.0). Anthropogenic emissions are those from the Greenhouse gas-Air pollution Interactions and Synergies (GAINS) model, and biomass burning emissions are from the Global Fire Emission Database (GFED v3, van der Werf et al., 2010). In CARMA, 20 size bins are used for both pure sulfate particles (bins from 0.2 nm to 1.3 μm in radius, only used up to 500 nm) and mixed aerosols composed of BC, primary and secondary OC, dust, sea salt, and sea-spray sulfate (bins from 0.05–8.7 μm in radius, again, only analyzed up to 500 nm). SOA formation is based on the VBS approach from Pye et al. (2010). The removal of OA occurs only by dry and wet deposition. Compared to the CESM2-SMP and CESM2-DYN simulations, the convective removal of aerosols uses the modified scheme described in Yu et al. (2019) which accounts for aerosol secondary activation from the entrained air above the cloud base, and the scavenging of activated aerosols in convective updrafts. The default CESM can transport aerosols from the cloud base to the top of the cloud in strong convective updrafts in one time step without scavenging them, while the new scheme allows for a more efficient removal off all aerosols inside convective clouds. A sensitivity simulation is performed for ATom-1 to quantify the effect of this improved removal on OA concentrations (Section 4.5).

2.2 AeroCom-II model climatology

The ATom measurements are also compared to the global model OA predictions generated within the Phase II Aerosol Comparisons between Observations and Models (AeroCom-II) project (Schulz et al., 2009). We consider the monthly average results of 28

global models, which is a subset of those presented in Tsigaridis et al. (2014), based on the availability of model results. It should be noted that the meteorological forcing used in these models is mostly based on the year 2006, while the anthropogenic and biomass burning emissions are mostly representative of the year 2000. For comparison purposes, the monthly mean model outputs for the months of August (ATom-1) and February (ATom-2) are interpolated along the flight path (latitude, longitude, and altitude), and averaged the same way as the measurements (see section 3.2).

3 Description of ATom measurements

3.1 Submicron aerosol data

The measurements of non-refractory submicron aerosols were performed onboard the NASA DC8 aircraft as part of the ATom field study (Wofsy et al., 2018) using the University of Colorado Aerodyne High-Resolution Time-of-Flight Aerosol Mass Spectrometer (AMS in the following, Canagaratna et al., 2007, DeCarlo et al., 2006).

We use measurements from both the NH summer (August 2016, ATom-1) and winter (February 2017, ATom-2) deployments. Figure 2a shows the flight path and the vertical extent of the ATom-1 dataset colored by OA mass concentrations (see Figure S1 for ATom-2). The aircraft performed systematic vertical sampling with ~140 vertical profiles per campaign throughout the troposphere from the near surface ~0.2 km to the upper troposphere/lower stratosphere region at ~13 km altitude. Details on the operation of the CU AMS on board the DC-8 are reported in Schroder et al. (2018), Nault et al. (2018), and Jimenez et al. (2019b). AMS data was acquired at 1 Hz time resolution and independently processed and reported at both 1 s and 60 s time resolutions (Jimenez et al., 2019a). The later product, with more robust peak fitting at low concentrations was exclusively used as the primary dataset in this work. Detection limits at different time resolutions/geographical bins relevant to this study are discussed in Section 3.3. The overall 2σ accuracies of the AMS measurement (38% for OA, 34% for sulfate and other inorganics) are discussed in Bahreini et al. (2008) and Jimenez et al. (2019b).

For ATom, the AMS reported the standard non-refractory aerosol species OA, sulfate, nitrate, ammonium, and chloride, with the response for all the nominally inorganic species characterized by in-field calibrations. In addition, it also reported methanesulfonic acid (MSA, Hodshire et al., 2019a describes the AMS MSA methods and calibrations for ATom) and sea salt for for D_{geo}<450 nm (based on the method of Ovadnevaite et al., 2012). Both

of these species were important to achieve closure with the volume calculated from the on-board sizing instruments in the marine boundary layer (Jimenez et al., 2019b). Another important refractory submicron species not captured by the AMS measurements is BC. This was measured on ATom with the NOAA SP2 instrument (Katich et al., 2018). It should be noted that aircraft measurements of aerosol mass concentrations are given in $\mu g\ sm^{-3}$ (i.e., under standard conditions of 1 atm and 273.15 K).

For ATom the AMS measured particles with geometric diameters (based on the campaign-wide average density of 1640 kg m^{-3}, Jimenez et al., 2019b) of between D_{geo}~60 and 295 nm with ~100% efficiency (and between 35 and 460 nm with 50% efficiency). Here we denote the AMS aerosol data as "submicron" mass (based on the more usual definition using aerodynamic diameter, which is larger than the geometric diameter; DeCarlo et al., 2004), with the assumption that non-refractory aerosol are small contributors to mass above the AMS size range. As shown in Brock et al., 2019, the accumulation mode for the ATom sampling environment only extended up to 500 nm, and hence, as expected for a background tropospheric environment, this approximation is appropriate. Very good agreement was observed with the integrated volume calculated from the number size distributions for ATom (Brock et al., 2019). A low bias compared to a typical submicron definition can occur in thick biomass burning plumes and in the lower stratosphere at times (Jimenez et al., 2019b). As detailed in Table 1, the accumulation mode for the bulk models discussed in this study overlaps with the size range of the AMS, and for the sectional models (CESM1-CARMA, GEOS-Chem-TOMAS, ECHAM6-HAM) only the bins that match the AMS size range were used. As expected based on the previous discussion, however, a comparison of the total OA calculated by these sectional models with the modeled OA inside the AMS size-range showed small differences (Slopes for ATom-1 linear regressions: CESM1-CARMA:0.91, GC10-TOMAS: 0.94, ECHAM6-HAM 1.00) mostly influenced by the high concentration points in the biomass plumes off Africa that have a large effect on the regression since they are about 10 times larger than the bulk of the dataset).

Refractory and non-refractory aerosol composition was also measured using the NOAA Particle Analysis by Laser Mass Spectrometry (PALMS) instrument. PALMS classifies individual aerosol particles into compositional classes including biomass burning (Hudson et al., 2004), sea salt (Murphy et al., 2019), mineral dust (Froyd et al., 2019), and others. Mass concentrations for these particles types are derived by combining PALMS

363 composition data with aerosol size distribution measurements (Froyd et al., 2019). Good
364 agreement overall was found for OA, sulfate and seasalt between the two particle mass
365 spectrometers during ATom once the AMS and PALMS instrument transmissions were
366 accounted for (Jimenez et al., 2019b). For all PALMS data used in this work (biomass
367 burning fraction and dust) the AMS transmission function was applied to ensure that both
368 instruments were characterizing approximately the same particle range.

369 For a particular airmass, the mass fraction of biomass burning (BB) aerosol reported by
370 the PALMS instrument $f(BB)_{PALMS}$ (Thompson and Murphy, 2000; Froyd et al., 2019) was
371 then used to evaluate the degree of BB influence. This parameter correlates quite well
372 with other gas-phase BB tracers, and is more useful as a particle tracer since its lifetime
373 follows that of the particles. Importantly, it is not impacted by the long lifetimes of the gas-
374 phase tracers (e.g. 9 months for CH_3CN) and unrelated removal processes (e.g. ocean
375 uptake for CH_3CN and HCN) that result in highly variable backgrounds. Hence $f(BB)_{PALMS}$
376 has a much higher contrast ratio and linearity for particle BB impacts, compared to the
377 available gas-phase tracers in the ATom dataset. An airmass was classified as non-BB
378 influenced when $f(BB)_{PALMS}$ was lower than 0.30 (Hudson et al, 2004) as shown in Figure
379 2b. For both ATom-1 and 2, about 74% of measurements were classified as not influenced
380 by biomass burning. $f(BB)_{PALMS}$ was also used to assess the impact of POA on the total
381 OA burden (next section); note that no thresholding was applied in that case.

382 ### *3.2 Estimation of the POA fraction for the ATom dataset*

383 For model evaluation purposes, it is important to know whether the source of OA is primary
384 or secondary. For ground studies close to sources (e.g. Jimenez et al., 2009) Positive
385 Matrix Factorization of AMS mass spectra (PMF, Ulbrich et al., 2009) can be used to
386 estimate the contribution of primary sources (mostly from transportation, heating, cooking,
387 and biomass burning) to total OA. This approach is not suitable for ATom. To accurately
388 resolve a minor factor such as POA in an AMS dataset, there needs to be a combination
389 of: (a) Sufficient OA mass concentration, so that the signal-to-noise of the spectra is
390 sufficient; (b) Enough fractional mass for the factor to be resolved (>5% in urban areas
391 per Ulbrich et al. (2009), probably a larger fraction at low concentrations such as in ATom);
392 (c) Sufficient spatio-temporal variability ("contrast") in the relative contributions of different
393 factors, since that is part of what PMF uses to extract the factors; (d) Sufficient difference
394 in the spectra of the different factors (for the same reason as (c)), and (e) relatively
395 invariant spectra for each factor across the dataset (as this is a key assumption of the

PMF algorithm). As an example of a near ideal case, in Hodshire et al (2019) we extracted MSA by PMF from the ATom-1 data, and were able to match that factor with our independently calibrated MSA species. A very distinct and nearly invariant mass spectrum was measured repeatedly near sources (MBL) (and was mostly absent elsewhere, thus providing strong spatio-temporal contrast) and accounted for about 6% of the fractional mass and 15% of the variance in time. Thus all the conditions were met. For POA, on the other hand, the air sampled in ATom and coming from e.g. Asia has POA and SOA very well mixed, with little change on their relative mass fractions vs. time (as the aircraft flies through that airmass). POA is very low, as documented later in this paper. Atmospheric aging makes the spectra from all OA sources more and more similar as measured by AMS spectra (Jimenez et al., 2009). Thus most of the conditions above are not satisfied for extracting POA by PMF analysis of this dataset.

Instead, in this work we have estimated POA based on the fact that it is co-emitted with BC as part of the combustion processes releasing both species in source regions, and that BC is not impacted by chemical aging processes over the lifetime of the airmass. Note that BC can physically age but it is not lost in any significant amount to the gas-phase due to chemical processes in the atmosphere. We assume non-differential removal (and transport) of the BC fraction relative to the rest of the POA (the two are generally internally mixed, Lee et al., 2015). Table S1 summarizes recent POA/BC and POC/EC emission ratio determinations for urban background sites, which best represent real mixes of pollution sources, and for individual sources of POA (from mobile sources – commonly referred as HOA – and cooking aerosol – COA). Based on Table S1 data, we assume POA to be co-emitted with BC for anthropogenic fossil fuel / urban region POA (herein called FF_{ratio} for simplicity, even though much of it is non-fossil, Zotter et al., 2014; Hayes et al., 2015) at a ratio of 1.5 (average of all urban ambient air studies that report POA and BC for best intercomparability to the ATom dataset; including all urban studies results in a very similar number, 1.48). Mobile source measurements in general exhibit lower ratios (POA/OA ratio 0.5-1.5) while COA determination typically ranges from 2 to 3. Hence, the ratio used here is a good estimate for a diverse mix of urban sources as appropriate for ATom. The studies used to derive the emission ratio used ambient data in urban air, where all sources mix together and impact the POA/BC ratio, and thus the ratios include the impact of POA sources that may not emit BC. It should be noted that urban model ratios do not include emissions associated with fugitive dust from road, tire and construction, as those are typically found in larger particles than those studied here (Zhao et al., 2017).

For biomass burning sources, we use a value of POA/BC = 11.8 (BB_{ratio}), based on the average of the recent review by Andreae (2019), which included over 200 previous determinations for a variety of fuels and burning conditions (since Andreae (2019) used and OA/OC ratio of 1.6 in his work, we have used that value to calculate POA/BC; we note that this is different from the 1.8 OA/OC ratio used for other studies listed in Table S1). We note the measured total OA/BC of ~3.5 (conservatively assuming that all OA is POA) observed on both ATom missions for the large African-sourced BB plumes over the Equatorial Atlantic. We note that using the larger BB_{ratio} from Andreae (2019) leads to a POA fraction >> 100% in the ATom African plumes. We also perform sensitivity studies with values of both FF_{ratio} and BB_{ratio} within the literature range.

The PALMS determined mass fraction of biomass impacted aerosol ($f(BB)_{PALMS}$) can then be used to determine a total POA contribution from both types of sources:

$$POA = [BC]*(FF_{ratio}+(BB_{ratio}- FF_{ratio})*f(BB)_{PALMS}) \quad \text{(Eq. 1)}$$

Further detail is provided in Table S2, which summarizes the POA/BC ratios used in the emission inventories implemented in current models. Overall, there is reasonable agreement with the measurements in Table S1, with FF_{ratio} ranging from ~0.5 for diesel fuels, to >2 for energy production and ~5 for residential emissions (which include some BB). On the other hand, for biomass burning, the emission inventories ratios range from ~5 for crop, to ~15 for forest, and up to ~50 for peatland. While generally consistent with the values discussed by Andreae (2019), they are on the lower end of the ranges discussed in that work. The averages and ranges of the measurement and model ratios are similar, and thus no significant model bias on the ratios is apparent.

PALMS detection efficiency increases with size across the accumulation mode, and therefore the f(BB) number fraction is weighted to the larger size end of the accumulation mode. In very clean regions of the upper troposphere (typically <0.15 μg sm^{-3} submicron mass) particles below the PALMS size range can contribute significantly to aerosol mass (Williamson et al., 2019; Jimenez et al., 2019b). If BB particles are not evenly distributed across the entire accumulation mode (due to preferential removal in convective updrafts of primary aerosol, cf. Yu et al., 2019 and Section 4.5; and preferential condensation of SOA on smaller particles), then the f(BB) reported by PALMS will be an overestimation. For the final analysis these periods where left in the dataset, and therefore for the LS the reported POA is likely overestimated for these regions, although their impact on the mass-weighted campaign average is negligible.

The contribution of POA from sea spray is difficult to constrain. As an order-of-magnitude estimate, marine POA is roughly calculated based on preliminary calibrations of OA on mineral dust particles from the PALMS instrument (personal communication K. Froyd). Using this calibration, the average OA by mass on sea salt was <10% for the large majority of MBL sampling (>85%). Since sea salt contributed 4% (11%) of mass in the AMS size range for ATom-1(2) (Figure 2), we estimate that marine POA is on the order of ~1% of aerosol mass in the AMS size range, and possibly much lower. Thus we think that it is reasonable to neglect the contribution of marine POA to this dataset. Future studies will refine this estimate.

3.3 Data processing for comparisons

For the comparisons between the measurements and the various global models, data were averaged both vertically and zonally to minimize the impact of smaller plumes or vertical gradients in aerosol concentrations that might not be captured by coarse resolution models. For the same reason, all data near airports was removed from the datasets prior to analysis (up to about 3 km on the climb in/out). In order to restrict this analysis to the remote troposphere, the last leg of the ATom-1 mission (over the continental US) was taken out of the dataset as well. Data was binned into 5 large latitude regions as shown in Figure 2a including southern polar (55-80°S, "S.Polar"), southern mid-latitudes (25-55°S, "S.Mid"), equatorial (25°S-25°N, "Equatorial"), northern mid-latitudes (25-55°N, "N.Mid"), northern polar (55-80°N, "N.Polar") and analyzed separately for the Pacific and Atlantic basins. For data in each of these latitude regions, altitude profiles were calculated with a constant 600 m altitude resolution. According to both variability in the cleanest air and statistical analysis of the organic background subtraction (Drewnick et al. 2009), the 1σ precision at low concentrations for one-minute data ranged between 20 and 50 ng sm^{-3}, or a 3σ detection limit between 60 and 150 ng sm^{-3} for the one-minute data (confirmed by frequent filter blanks). Per standard statistics, the precision of a measurement decreases (i.e., gets better) with the square root of the number of points (or time interval) sampled. I.e. the precision of an average can be approximated by the standard error of the mean (σ/sqrt(*n*), where *n* is the number of measurements averaged), and it is better than the precision of the individual data points (σ). This also applies to the detection limit, since it is just 3 times the precision. Note that a detection limit is not meaningful unless the averaging time is specified. For example let's assume that the detection limit is 20 ng m^{-3} (1-second), and the data points over 60 consecutive seconds are all 10 ng m^{-3}. All 1-

second measurements are below the 1-second DL. However the average (10 ng m^{-3}) is now above the DL for 1-minute averages, which is 20/sqrt(60) = 2.6 ng m^{-3}. On average, each individual point in the profiles represents the average of about 25 min of ATom flight data. At that time resolution, the OA 1σ precision was about 10 ng sm^{-3}. Hence with very few exceptions (10 points for both missions combined), the OA concentrations in the averaged profiles reported are well above the instrumental detection limit in those regions. For model-measurement comparisons along flight tracks, model outputs and measurements were considered at 1-minute time resolution, which corresponds to ~0-700 m vertical resolution and ~0.05-0.15 degrees horizontal resolution. Note that a large fraction of the 1-minute OA values in the remote free troposphere were below the local 3σ detection limit. The data of periods of zero concentration (sampling ambient air through a particle filter) do average to zero. Some negative measurements are present, and this is normal for measurements of very low concentrations in the presence of instrumental noise. Averaging of longer periods, as done for the figures in this paper, reduces the detection limit. We therefore caution future data users that the reported data should be averaged as needed, as replacing below-detection limit (or negative) values by other values introduces biases on averages. For fractional ratio analysis, measurements were averaged to 5-minute time resolution to reduce the noise in the ratios due to noise in the denominator. The results are not very sensitive to the 5-minute averaging (compared to 1-minute) as shown in Figure S12 for OA to sulfate ratios. The same figure also illustrates that excluding ratios affected by negative concentrations (the non-bracketed case, overall these are about 15% of the dataset) does not really affect the fractional distribution, with the variance between the two cases diminishing as the averaging interval increases. To further confirm that there is no inherent bias in the fractional products regardless of the treatment of low concentration values, an additional sensitivity analysis was performed where data was filtered by an independent measurement proxy for aerosol mass, the aerosol volume measured in ATom (Brock et al., 2019). Using a range of value that encompasses the regime where the AMS calculated volume to aerosol measured volume exhibited increased noise (Jimenez et al., 2019b), no systematic bias was found (Figure S13), with variations of about 10% in fractional volume for different filtering conditions.

Some of the performed analysis required separating the dataset into vertical subsets. In this manuscript, we define the marine boundary layer (MBL) as the region below 1.5 times the calculated boundary layer height in the NCEP global model reanalysis. The free troposphere (FT) includes all data points between the top of MBL and the NCEP

tropopause height, and the LS region includes all points above the NCEP tropopause height. The tropopause height varied during ATom between 8 and 16.5 km; given the DC-8 ceiling (42 kft, 12.8 km) the stratosphere was only sampled at latitudes higher than 30 degrees in both hemispheres. The MBL height varied between up to 1.5 km in the mid-latitudes, ~1 km in the tropics, and sometimes <150 m (lowest DC-8 altitude) for some of the sampling in the polar troposphere.

3.4 Submicron aerosol composition

Figure 2b shows that during both NH summer and winter ATom deployments, OA is one of the three dominant components of the measured submicron aerosol in the remote troposphere, together with sulfate and sea salt. During ATom-1, average submicron aerosol concentrations were close to 0.8 $\mu g\ sm^{-3}$ in the marine boundary layer and biomass burning outflow regions, and ~2 times lower in the free troposphere and lower stratosphere regions. ATom-2 had overall lower average concentrations below 0.4 $\mu g\ sm^{-3}$ (vs. 0.5 $\mu g\ sm^{-3}$ for ATom-1). As expected, sulfate (sulfuric acid in the lower stratosphere) is the dominant constituent in the MBL (~50%) and LS (50-70%), while the OA contribution is generally below 10% and 40%, respectively in those regions. A large fraction of sea salt aerosol is found in the MBL especially during the NH winter deployment (~30%, see Murphy et al., 2019).

OA is found to be a major constituent (~50%) of submicron aerosol in the clean (non-BB influenced) free troposphere. The contribution of OA is 1.4 times larger than that of sulfate during the NH summer, and 1.2 times lower than that of sulfate during the NH winter, which is likely due to a large contribution of the NH sources to SOA production in the NH summer. Biomass-burning events increase the OA contribution relative to that of sulfate, and lead to a higher contribution of OA to total during the ATom-1 mission (stronger BB influence).

3.5 Spatial and vertical distribution of OA

Figure 2a (and Fig. S1) shows the spatial and vertical distribution of OA mass concentrations measured during ATom-1 (and ATom-2) campaigns. Most data were taken over remote oceanic regions (and a few remote continental regions, primarily over the Arctic). The measured OA varies between extremely clean conditions (< 0.1 $\mu g\ sm^{-3}$) encountered mostly in the Pacific and Southern Ocean regions and moderately polluted conditions (> 2 $\mu g\ sm^{-3}$) in the biomass burning outflow regions. During ATom-1 (August

562 2016), a strong BB influence is observed in the lower troposphere (below 6 km) over the
563 Atlantic basin off the African coast and over California with OA concentrations exceeding
564 10 μg sm^{-3}. OA associated with biomass burning is also present in the upper troposphere
565 over equatorial regions and over Alaska, associated with the deep convective transport of
566 biomass burning aerosols. The biomass burning contribution to carbonaceous aerosols in
567 those regions during ATom-1 was also apparent in the black carbon measurements
568 (Katich et al., 2019). ATom-2 was generally less polluted than ATom-1, likely due to a
569 more limited global influence of biomass burning emissions during that period, and also to
570 a less active photochemistry during winter months in the NH.

571 The measured OA is characterized by a strong latitudinal gradient. Figure 2c shows the
572 average vertical profiles of measured OA over the selected latitudinal bands during August
573 2016. The cleanest airmasses are observed over the remote oceanic regions of the
574 Southern Hemisphere (SH, 25-80°S) with OA mass concentrations below 0.06 μg sm^{-3}.
575 These extremely low OA concentrations can be explained by the very low influence from
576 continental emission sources, and presumably low marine POA and SOA precursor
577 emissions. This is consistent with low concentrations of gas-phase pollutants (e.g. CO,
578 ethane, propane). An enhancement can be noticed above 10 km in the lower stratosphere.
579 In some cases, this could be related to the long-range transport of biomass burning
580 aerosols from the tropics. By comparison, the Arctic region is more polluted with an order
581 of magnitude higher OA levels compared to its analog of the SH (i.e. OA loadings ranging
582 from 0.1 to 0.5 μg sm^{-3}). These concentrations are comparable to FT levels measured in
583 the extratropical regions (25-55°N) of the NH. The equatorial marine regions (25°S-25°N)
584 display the highest OA concentrations with a strong gradient between lower and upper
585 troposphere. In the lower troposphere OA, concentrations are close to 1 μg sm^{-3}, and
586 decrease down to 0.1 μg sm^{-3} at altitudes above 4km. The highest OA levels are
587 associated with the African outflow over the southeastern Atlantic Ocean, which results
588 from the transport of the biomass burning smoke from the sub-Saharan regions and
589 increasing urban and industrial air pollution in southern West Africa (Flamant et al., 2018).
590 Figure 2d shows that the Atlantic basin is often more polluted than the Pacific basin, not
591 only because of the African biomass burning influence but also due to the contribution of
592 anthropogenic pollution in the lower troposphere of the NH. It should be noted that Asian
593 pollution was likely an important contributor to the North Pacific Basin, especially between
594 2 and 6 km, in both ATom deployments (see figures 2a and S1). Several-fold higher OA

concentrations are found near the surface (below 1km) over the southern Pacific compared to that same location in the southern Atlantic, which could be indicative of the stronger emission of marine OA in the Pacific basin.

In addition to spatial gradients, a strong summer-to-winter contrast is observed in OA concentrations. Figure 2e shows the ratio between OA vertical profiles measured in the NH summer ATom-1 vs. in the NH winter ATom-2. The NH is more polluted during the NH summer due to the photochemical production of SOA, as well as biomass burning emissions, leading to the tripling of OA concentrations in the extratropical regions (25-80°N) on average regardless of altitude. The doubling of OA loading in the lower troposphere at the equator (25°S-25°N) in the NH summer (August, ATom-1) is strongly influenced by the biomass burning activity in the sub-Saharan African region as already mentioned above. Likewise, OA concentrations are found to be generally higher in the SH during the SH summer. These zonal trends are broadly similar to the ones described in Katich et al (2018) for BC.

4 Model-measurement comparisons

4.1 Evaluation of predicted OA concentrations

Prior to evaluating model performance in simulating OA, we have assessed the ATom models' ability to simulate sulfate aerosols. According to the model evaluation shown in Table S3, the predicted sulfate concentrations are generally within 40% of the measured values, which is comparable to the AMS measurement uncertainties. The only exception is found for the ECHAM6-HAM model, which overestimates sulfate aerosols by a factor of two. These results imply that most ATom models capture relatively well the overall sulfate burden. However, large root mean square error (RMSE > 0.4 μg sm^{-3} for ATom-1 and > 0.2 μg sm^{-3} for ATom-2) is indicative of their limited skill in reproducing the observed variability in sulfate concentrations.

For OA, model evaluation metrics for the entire ATom-1 and ATom-2 campaigns are given in Table 2 for the eight ATom models and their ensemble, as well as the AeroCom-II ensemble. The results show that the normalized mean bias is substantially lower for the ATom model ensemble compared to AeroCom-II decreasing from 74% to 4% for ATom-1 and from 137% to 23% to ATom-2, which is within the measurement uncertainty range. The mean temporal correlations are substantially improved from 0.31 (0.38) for AeroCom-II to 0.66 (0.48) for ATom model ensemble during ATom-1 (ATom-2). However, results

vary strongly among ATom models. Models using prescribed emissions of non-volatile SOA have the tendency to overestimate the OA concentrations during both NH summer and winter deployments (with ~35-60% overestimation for CESM2-SMP, ~70-100% for ECHAM6-HAM, and up to 150% for GC10-TOMAS during ATom-2), with the exception of the GEOS5 model that on the contrary underestimates OA concentrations by 5-25%. During the NH summer (ATom-1), models using the VBS parameterization from Pye et al. (2010) tend to underpredict the OA concentrations by 43% for GC12-REF and 33% for CESM1-CARMA for ATom-1, most likely due to the excessive evaporation of the formed SOA in remote regions and low yields for anthropogenic SOA (Schroder et al., 2018; Shah et al., 2019). Models using the VBS parameterization from Hodzic et al. (2016) (CESM2-DYN and GC12-DYN) where OA is less volatile and also OA yields are corrected for wall losses show an improved agreement with observations especially for CESM2-DYN (with NMB of ~5%), and to a lesser extent for GC12-DYN (NMB of ~33%). During the NH winter (ATom-2) characterized by a lower production of SOA, both VBS approaches lead to an overestimation of the predicted OA. This is likely caused by excessively high levels of primary emitted OA as discussed in section 4.4.

Figure 3 compares the average median ratios between modeled and observed OA concentrations for the ATom and AeroCom-II model ensembles for different regions (BB, MBL, FT, LS). The results show that the median ratio for the ATom model ensemble is close to unity in all regions. This is at least a factor of two improvement compared to AeroCom-II models, which were almost always biased high for the remote regions sampled in ATom. The model spread has also been reduced by a factor of 2-3 in all regions. This reduction in the ensemble spread may partially be explained by a smaller size of the ATom model ensemble (see Fig. S2), which also includes models with a more up-to-date OA representation. In order to explore this point further, results for a subset of AeroCom-II models (using earlier versions of models in the ATom ensemble) show only a slight reduction (~10%) in the model spread, with however some regional differences i.e. an improved agreement with observations in the MBL, but an increase in the model bias and spread in the LS (Figure S2). Thus, model improvement for the more recent models appears to be the main reason for the reduced spread.

4.2 Evaluation of predicted OA vertical distribution

Figure 4 compares the mean vertical profiles of OA measured during ATom-1 and -2 with the predictions of the model ensemble average based on the eight ATom models (Table

1) and 28 AeroCom-II models for the different latitudinal regions of the Pacific and Atlantic basins. Note that the use of a wide logarithmic scale (to be able to span all the observations) may make the observed differences appear small, although they often reach factors of 2-10 and larger (Figure S5 shows the results on a linear scale). For AeroCom-II, large latitudinal differences exist in the results with a better performance closer to source regions and large disagreement in the lower stratosphere and remote regions, as already suggested by the mission medians shown in Figure 3. The best AeroCom-II model performance is found over the equator in both basins, where the model ensemble captures within a factor of 2 the observed OA concentrations throughout the troposphere in the Pacific basin, and matches remarkably well the observations in the lower troposphere of the Atlantic basin that is heavily influenced by biomass burning emissions. Reasonable agreement is found for the OA vertical distribution over the NH Atlantic and Pacific oceans, especially in the lower troposphere (< 4 km). The largest model discrepancies (1-2 orders of magnitude) are found in the remote regions of the Southern Ocean and SH mid-latitudes during both seasons and basins. The model overestimation is also large over the NH mid-latitude Pacific basin in the upper troposphere. A spread of 2-3 orders of magnitude is observed around the ensemble average indicating a very large variability in individual model predictions. This evaluation of AeroCom-II models in remote regions is an extension of that performed at the surface for urban and remote stations by Tsigaridis et al. (2014) (as in that previous study, the data and model simulations compared are not synchronous in time). The tendency of the model ensemble to overpredict OA concentrations by a factor of 2 on average in the remote regions is consistent with the transition from the large underprediction in OA near the source region to a slight overprediction of OA in remote continental sites that was reported for most AeroCom-II models (Tsigaridis et al., 2014), and also observed for default parameterizations in other studies (Heald et al., 2011; Hodzic et al., 2016).

By comparison, the results of the ATom model ensemble show a much better agreement with observations. The model spread is still substantial, but mostly below a factor of 5. Figures S6 and S7 show OA vertical profiles for individual ATom models and the spread in their results. In most regions, the ATom model ensemble captures reasonably well both the absolute concentrations as well as the shape of the vertical profiles. In the biomass burning outflow and NH mid-latitude regions, the ATom ensemble average better captures the higher OA concentrations in the boundary layer and lower OA concentrations in the lower stratosphere than the AeroCom-II ensemble. We note that using the ensemble

694 median OA profiles instead of ensemble mean OA profiles (as shown in Figure 5 and S7)
695 results in a slightly lower values of OA but does not change the conclusions of the model-
696 measurement comparisons (Figure S18).

697 ### *4.3 Oxidation level of organic aerosols (OA/OC ratios)*

698 In addition to OA mass concentrations, we also evaluate the model's ability to simulate
699 their degree of oxygenation, an indicator of their oxidation and aging (Aiken et al., 2008;
700 Kroll et al., 2011). Ambient measurements of the oxidation level of organic particles are
701 limited (Aiken et al., 2008, Canagaratna et al., 2015), and the ATom dataset provides the
702 first global distribution of O/C and OA/OC ratios for the remote aerosol. The OA/OC ratio
703 is an estimate of the average molecular weight of organic matter per carbon weight, and
704 it mostly depends on the oxygen content (i.e. the O/C ratio), in the absence of significant
705 concentrations of organonitrates and -sulfates. It is needed to compare measurements of
706 organic aerosol mass (from e.g. AMS) with organic carbon measurements (from e.g.
707 thermooptical methods). It is also needed to compare the various types of measurements
708 to model concentrations, which are sometimes carried internally as OA and sometimes as
709 OC. A low OA/OC ratio is indicative of freshly emitted OA from fossil fuel combustion
710 (typically ~1.4), and its value increases with increased processing of organics in the
711 atmosphere. Figure 5 shows that in the remote regions the bulk of measured OA/OC
712 ratios during ATom-1 and -2 range between 2.2 and 2.5, and are larger than values of 2.1
713 $\pm$ 0.2 found in the polluted US continental outflow regions that were sampled during
714 SEAC4RS, WINTER and DC3 field campaigns (Schroder et al., 2018). These values
715 indicate that remote OA is highly oxidized and chemically processed.

716 Note that for organosulfates (R-O-SO_2H and organonitrates (R-O-NO_2, p$RONO_2$ in the
717 following) only one oxygen is included in the reported OA/OC, as the fragments of these
718 species are typically the same as for inorganic species in the AMS (Farmer et al., 2010).
719 However in ATom organosulfates are estimated to account for ~1% of the total sulfate
720 (based on PALMS data, see Liao et al., 2015 for the methodology). Since sulfate and OA
721 concentrations are comparable, organosulfates would only increase the OA/OC by ~1%
722 on average. Organonitrates are reported from the AMS for ATom. Their impact on OA/OC
723 is not propagated for the default values, to maintain consistency with a large set of OA/OC
724 measurements by AMS in the literature, and since they would increase OA/OC on average
725 by only 4.5% (ATom-1) and 2.2% (ATom-2), which is smaller than the uncertainty of this

726 measurement. However, we show the results with both methods in Fig. 5 to fully document
727 this topic.

728 Importantly, this ratio is also used to calculate the total OA mass concentration for models
729 that provided their outputs in terms of organic carbon concentrations ($[OA]_i = [OC]_i$ x
730 OA/OC_{ratio}). Most Models use a constant OA/OC ratio, but the value used varies
731 substantially. OA/OC of 1.4 is used in ECHAM6-HAM, whereas 1.8 is used in GEOS5 and
732 GC10-TOMAS simulations for both POA and SOA. Other models calculated directly SOA
733 concentrations without applying this conversion (CESM1-CARMA, CESM2-SMP, CESM2-
734 DYN, GC12-REF and GC12-DYN), but for POA used the ratio of 1.8 (CESM1-CARMA,
735 CESM2-SMP, CESM2-DYN) and 2.1 (GC12-REF and GC12-DYN). Most of the AeroCom-
736 II models used the ratio of 1.4 for all primary and secondary OA (Tsigaridis et al., 2014).
737 The comparison with measurements shows that the measured values are ~40% larger
738 than those assumed in some of the ATom models, and 60-80% larger than used in
739 AeroCom-II models. The comparison between the observed and predicted OA/OC vertical
740 profiles (Fig. S3) shows that AeroCom-II models tend to generally underpredict this ratio,
741 and do not capture its increase in remote regions. As a result, this underestimation of
742 OA/OC ratios and the use of a constant value could substantially impact the comparisons
743 of OA mass concentrations for several models considered in this study (ECHAM6-HAM,
744 GEOS5, CESM1-CARMA and GC10-TOMAS). If we correct for the underestimated
745 OA/OC ratio using the ATom measured values of 2.2 (to be conservative) and compare
746 to previously discussed biases in Table 2, the overprediction of the ECHAM6-HAM model
747 is increased to ~110-160%, and that of GC10-TOMAS to 180% during ATom-2 while
748 having ~15% bias in ATom-1, whereas GEOS5 results now overestimate up to 30% during
749 ATom1, and perform much better during ATom-2.

750 These results demonstrate that current global chemistry-climate models use unrealistically
751 low OA/OC ratios, which results in a large underestimate of the degree of oxidation of OA
752 in remote regions. Inaccurate prediction of OA oxidation as it ages could impact not only
753 the calculations of OA burden, but also its optical properties as the absorption of OA
754 changes with its degree of oxidation (through the formation and destruction of brown
755 carbon, Laskin et al., 2015, Forrister et al., 2015). However, models used in this study did
756 not include these effects.

4.4 Contribution of primary vs. secondary OA

We further assess whether global models can adequately predict the relative contributions of primary and secondary OA. We strive to quantify these fractions with the most straightforward methods (with the fewest assumptions) for both models and measurements. POA concentrations were estimated from the BC measurements by using an emission ratio appropriate to the airmass origin (biomass burning vs. anthropogenic), and using the f(BB) mass fraction from the PALMS single particle instrument (see Section 3.2). By using the POA/BC ratio at the source regions after most evaporation, but before POA chemical degradation evaporation has taken place, we implicitly assume POA to be chemically inert, while in reality it can slowly be lost to the gas-phase by heterogeneous chemistry (e.g. George and Abbatt, 2010; Palm et al., 2018). Thus, the observation-based method provides an upper limit to the fraction of POA. The model/measurement comparison is only shown for the CESM and GEOS-Chem model variants, as other participating models do not separate or did not report their POA and SOA fractions. In all simulations, POA was treated as a chemically inert directly emitted primary aerosol species that only undergoes transport, transformation from hydrophobic to hydrophilic state with ageing (1-2 days typically), coagulation, and dry and wet deposition. Importantly, the treatment of POA as non-volatile (rather than semi-volatile) in models is fully consistent with the assumptions for POA estimation from the measurements.

Figure 6 compares the vertical profiles of measurement-derived POA during ATom-1 and predicted by the CESM2-DYN model over clean remote regions of the Pacific basin and northern polar Atlantic that are not influenced by biomass burning. Comparisons for other models are similar (not shown). Observations show that POA is extremely small in remote regions, whereas the model predicts that about half of the OA is made of POA in those areas. Although the model reproduces quite well the measured total OA, it tends to severely overpredict the amount of POA and underpredict that of SOA over clean remote regions (with the two errors canceling each other when it comes to total OA). Over the biomass burning regions (not shown here) it can be difficult to directly quantify POA and SOA with this method, as total OA remains about constant, while POA decreases with aging and SOA increases (Cubison et al., 2011; Jolleys et al., 2015; Hodshire et al., 2019b). However, given this evolution the method used here would lead to an overestimate of POA for this reason.

A more general comparison is made in Figure 7, using the frequency distributions of the measured and simulated fraction of POA/OA, for the free troposphere only (Figure S8 shows the corresponding cumulative distributions). Observations indicate that most remote FT airmasses contain less than 10% POA, except for biomass burning plumes that are considered mostly primary. A slightly higher proportion of POA is seen in ATom-2, which is consistent with a slower photochemical production of SOA during NH winter. These results indicate that the remote OA is consistently dominated by SOA regardless of the season and location. The comparison with models reveals a very large discrepancy in the predicted vs. measured POA vs. SOA contributions. Models have a general tendency to severely overpredict the fraction of POA and underpredict that of SOA, displaying a much wider frequency distribution than the measurements (as also shown for POA and SOA vertical profiles for individual models on Figures S6 and S7). In GC12-REF, CESM2-DYN and CESM1-CARMA (without improved in-cloud removal) predictions for ATom-1, more than a half of the remote OA is POA, while that is very rarely observed in the free troposphere (possibly only during strong biomass burning events). Most models fail to reproduce the overwhelming dominance of SOA that is inferred from the measurements during ATom-1, while the discrepancies are less severe during NH winter (ATom-2). These seasonal differences suggest that model errors could be partially due to inefficient production of SOA, although removal errors also probably play a major role (see next section).

The differences are so large that they are pretty insensitive to details of the POA estimation method from the measurements, mostly because for the vast majority of the ATom track BC/OA ratios were extremely low and hence the exact magnitude of the multiplicative factor is secondary to the estimation of POA (Figure S11). As Figure S9 illustrates, the choice of FF_{ratio} has very little impact on the overall distribution of POA. On the other hand, while the BB_{ratio} does impact the overall distribution of POA, it mostly affects the points in the vicinity of the large Atlantic plumes. Since the POA/BC ratio in those plumes is fairly low, (see Section 3.2), using a very large BB_{ratio} mostly leads to an increase of the fraction of the points where POA > 100%. While the large range of published BB_{ratio} for different sources precludes a more accurate estimation by our method, for the purposes of the comparison with the model results we emphasize that even using the largest BB_{ratio}, fraction of SOA is still significantly larger in the ATom dataset that in any of the models.

Additional sensitivity tests were performed to investigate the impact of noisy data and uncertainties of f(BB) on the estimation of POA. Figure S11 clearly shows that the impact of a misattribution of the aerosol type by the stated PALMS uncertainty (Froyd et al., 2019) is completely negligible. Figure S10 details how the choice of averaging interval (with longer averaging times reducing both the fraction of OA measurements under the DL and below zero) impact the distribution of POA. Overall, no large changes are observed for averaging times >5 min, and hence a 5 min averaging interval was used for the analysis in Figure 7. Figure S10 also illustrates how capping the histogram impacts the POA distribution. To capture the most realistic $f_{(POA)}$ distribution, the data in Fig 7 was capped at the extremes (so $f_{(POA)}<0$ is taken as $f_{(POA)}=0$, and $f_{(POA)}>1$ is taken as $f_{(POA)}=1$). As Figure S10 shows, data with $f_{(POA)}<0$ is almost exclusively due to very small (and always positive, since BC cannot go negative) POA values being divided by small, negative noise in total OA, and hence treating that fraction of the histogram as essentially fPOA~0 is justified. On the other end of the distribution, data where POA is larger than OA is mostly due to our average BB_{ratio} being larger than the one encountered in most of the BB plumes in ATom. Choosing a lower BB_{ratio}, as Figures S9b and S9d illustrate, leads to $f_{(POA)}>1$ basically trending to zero, confirming our interpretation. This is a limitation of the dataset, and it does not seem appropriate to remove these points, since some fraction are likely dominated by POA. However, it shows that the POA estimation, especially for this part of the distribution likely overstates the importance of POA.

A comparison between simulations that have the same treatment of POA, and only differ in their chemistry and removal of SOA (e.g. CESM2-SMP vs. CESM2-DYN; GC12-REF vs. GC12-DYN) indicate that a more complex SOA treatment does not always result in a more accurate simulation of the primary/secondary character of OA, a result that was also found in the AeroCom-II multi-model intercomparison (Tsigaridis et al., 2014).

Finally, we have examined whether the non-volatile treatment of POA in models could lead to these unrealistically high POA fractions in the remote regions. Figure S16 shows a comparison of POA vertical profiles as predicted by the GC12-REF simulations that use non-volatile POA and a sensitivity simulation GC12-REF-SVPOA that uses semi-volatile POA similar to the standard treatment in GEOS-Chem as described in Pai et al. (2020). Note, however, that Pai et al. (2020) included marine POA emissions, used different reanalysis meteorology, and a different model version (12.1.1 rather than 12.0.1 here), so their resulting comparisons to ATom measurements are somewhat different than found

here for GC12-REF-SVPOA. The comparison indicates that the POA concentrations increase substantially in most regions when the semi-volatile POA parameterization is used. These results suggest that non-volatile treatment of POA is not responsible of the model bias.

4.5 Sensitivity to OA formation and removal

In this section, we further investigate some of the possible reasons for the incorrect model predictions of the relative contributions of POA and SOA in remote regions. Given the tendency of models to underestimate OA close to anthropogenic source regions and overestimate OA downwind in past studies (e.g. Heald et al., 2011; Tsigaridis et al., 2014; Hodzic et al., 2016), in this section we investigate the sensitivity of OA to increasing sources and increasing removals. We have performed two additional model simulations to test the sensitivity of the POA/SOA fractions to uncertainties in the representation of (i) wet scavenging, based on the CESM1-CARMA simulations in which we have removed the improvements in the aerosol removal by the convective updrafts (Yu et al., 2019); and of (ii) SOA formation based on the GC12-REF simulations in which we have replaced the SOA formation VBS mechanism (Pye et al., 2010) by an updated VBS mechanism that uses chamber wall-loss corrected SOA yields (Hodzic et al., 2016, same formation scheme that is used in GC12-DYN and CESM2-DYN runs, but with removals kept identical to GC12-REF). The results of these two sensitivity simulations are displayed on Figure 8, which shows measured and predicted mass concentrations of OA, POA, SOA and sulfate for ATom-1 as a function of the number of days since the air mass was processed through convection. One should keep in mind that this is an averaged plot that included airmasses from various regions and altitudes, and not a Lagrangian plot following the same airmass.

Sensitivity to in-cloud scavenging in convective clouds. Inefficient wet removal of primary OA could contribute to the POA overprediction in global models, especially in the tropics. Previous global model studies have reported two to three orders of magnitude overestimation of primary carbonaceous species such as BC in the free troposphere when the removal in the convective updrafts was not included (e.g. Schwarz et al., 2013, Yu et al., 2019). A strong reduction due to convective removal is also expected for POA concentrations, as POA is a primary species co-emitted with BC at the surface and internally mixed with it (Lee et al., 2015), and that is typically coated by secondary inorganics and organics over short timescales (Petters et al., 2006; Jiang et al., 2010; Wang et al., 2010). Figures 7a and 8 compare the simulations of CESM1-CARMA with

and without improved convective in-cloud scavenging during ATom-1. The improved in-cloud scavenging scheme considers aerosol activation into cloud droplets from entrained air above the cloud base, which is more realistic and results in a more efficient removal of aerosols in the upper troposphere by convection. E.g. a two order of magnitude reduction in BC in the upper FT was reported by Yu et al. (2019), resulting in much improved agreement with observations. Similar results were observed for sea salt aerosols in Murphy et al. (2019). Figure 8 shows that all submicron aerosol species simulated in CESM1-CARMA are strongly impacted by the in-cloud removal above the cloud base. POA concentrations are reduced by an order of magnitude while sulfate is reduced by 30% leading in both cases to a much-improved agreement with observations. SOA is reduced by ~30% as well, which leads to an underprediction of measured SOA concentrations. The overall impact on OA concentrations is a significant reduction, which leads to ~20% underestimation of OA in the aged remote air during ATom-1.

For the CESM2-DYN model that does not have improved in-cloud removal, the reasonable agreement (within 20%) with the observed OA concentrations thus results from coincidental error compensation between the overpredicted POA and underpredicted SOA. The prescribed SOA formation and the artificial 50% adjustment of SOA emissions based on Liu et al. (2012) in CESM2-SMP leads to an overestimation of observed SOA in aged remote airmasses.

Sensitivity to SOA formation. In addition, we have also tested the sensitivity of the OA composition to the choice of the SOA formation mechanism. Figure 8 compares the results of the GC12-REF model that uses SOA formation yields derived from traditional chamber experiments (Pye et al., 2010) and those corrected for loses of organic vapors onto chamber walls as proposed in Hodzic et al. (2016). Previous studies have reported that chamber wall losses could lead up to a factor of 4 underprediction of formed SOA (Zhang et al., 2014; Krechmer et al., 2016). It should be noted that in both cases, isoprene-SOA is formed in aqueous aerosols following Marais et al. (2016). The comparison shows a factor of 3 increase in SOA concentrations when the updated SOA formation is considered leading to a much better agreement with the observed SOA as well as the observed total OA. GC12-REF predicts well the amount of POA and overpredicts somewhat the amount of sulfate aerosols, which is expected as it already includes the improved aerosol removal in convective updrafts (Wang et al., 2014). Figure S6 also shows that POA vertical distribution is well captured in GEOS-Chem in most regions, except over the polar north

Pacific. It should be noted that these results are consistent with the POA/OA frequency distribution shown in Figure 7 (the POA/OA ratio predicted by GC12-REF is larger than the measured ratio, which is consistent with the fact that POA is about the right amount, and OA is underpredicted in Figure 8).

These sensitivity simulations suggest that a stronger convective removal of POA and a stronger production of SOA might be needed to correctly represent not only the total OA concentrations but also its primary and secondary nature in remote free troposphere and remote ocean regions. Accurate predictions of the OA concentration, composition, and source contributions for the right reasons are key for accurately predicting their lifecycle and radiative impacts. Only when there is confidence that the sources are accurately predicted, we can have confidence in OA predictions for pre-industrial and future conditions, as well as to evaluate PM mitigation strategies.

4.6 OA and sulfate relative contributions in FT

Finally, we assess the model ability to predict relative amounts of OA and sulfate in the free troposphere where they are the two major constituents of the submicron aerosol (Figure 2b). Accurate predictions of their relative contributions are crucial to determine the hygroscopicity of the submicron aerosol, and its ability to serve as a cloud condensation nuclei (CCN) in the remote free troposphere (Carslaw et al., 2013; Brock et al., 2016).

Figure 9a compares the average measured relative fractions of sulfate (36%) and carbonaceous aerosols (OA=59% and BC=5%) in the FT with those predicted by individual models during ATom-1. The CESM2 models best reproduce the observed relative contributions, with a slight underestimation of OA (57% instead of 59%) for CESM2-DYN, and a slight overestimation of OA (63% instead of 59%) for CESM2-SMP. GEOS5 has 15% more OA relative to sulfate than observed. All other models underestimate both OA and BC relative fractions. For instance, in GC12-REF and -DYN, both the BC and OA fractions are ~40% (relative) lower than observed.

Figure 9b shows the frequency distribution of observed and predicted fractions of OA relative to sulfate during ATom-1 and -2 in the free troposphere. Most models fail to reproduce the relatively uniform nature of the observed distributions during ATom-1, with typically narrower model shapes around a preferred ratio. The NH summer measurements indicate that OA > sulfate in ~55% of the samples (consistent with Fig. 2b), while models generally tend to underestimate the relative OA contribution. In particular, GEOS-Chem

and ECHAM6-HAM tend to overestimate the relative contribution of sulfate. A better agreement is found for GEOS5, CESM1-CARMA and CESM2-DYN, which follow more closely the shape of the observed distribution. The comparisons also suggest that the more complex SOA treatment of SOA formation and removal proposed by Hodzic et al. (2016) in the same host model leads to an improved agreement with observations (e.g. CESM2-DYN vs. CESM2-SMP; GC12-DYN vs. GC12-REF). It should be noted that CESM2-SMP uses fixed SOA yields that were increased by 50% as suggested by Liu et al. (2012), leading to an overestimation of the relative contribution of OA compared to that of sulfate in the free troposphere. During the NH winter (ATom-2), measurements show a somewhat higher proportion of sulfate aerosols (vs. ATom-1), which is consistent with a slower production of SOA in the NH during winter and a reduced influence of biomass burning. Similar conclusions are found for the evaluation of different models. It is worth mentioning that the comparison performed for the whole ATom-1 and 2 dataset (not shown) leads to similar results with even slightly stronger overestimation of the sulfate relative contribution compared to OA.

The discrepancies between the observed and predicted composition of submicron aerosol over remote regions can be quite large for other constituents as well. Figure 10 shows the comparison of measured and predicted composition of the submicron aerosol over the Southern Ocean (during the NH winter) where the disagreement in simulated sea salt, nitrates, ammonium, and MSA often exceeds the contribution of OA. While the observations show a more uniform distribution of non-marine aerosol with higher values in the mid and upper troposphere, respectively, most models tend to simulate highest fractions of OA (and sulfate) towards the tropopause. This may also be explained by the uncertainties in modeled wet removal of aerosol that has been discussed above. Specific studies have discussed and continue to investigate the ATom measurements and simulations of different components in more detail, including particle number (Williamson et al., 2019), black carbon (Katich et al., 2018; Ditas et al., 2019), MSA (Hodshire et al., 2019), sulfate-nitrate-ammonium (Nault et al., 2019), and sea salt (Yu et al, 2019; Bian et al., 2019; Murphy et al., 2019).

5 Conclusions and implications

Our understanding and representation in global models of the lifecycle of the OA remain highly uncertain, especially in remote regions where constraints from measurements have been very sparse. We have performed a systematic evaluation of the performance of eight global chemistry climate models and of 28 AeroCom-II models in simulating the latitudinal and vertical distribution of OA and its composition in the remote regions of the Atlantic and Pacific marine boundary layer, free troposphere and lower stratosphere, using the unique measurements from the ATom campaign. Our simulations are conducted for both ATom-1 and ATom-2 deployments that took place in August 2016 and February 2017, respectively. The main conclusions of the comparison are as follows:

- The AeroCom-II ensemble average tends to be biased high by a factor of 2-5 in comparison to measured vertical OA profiles in the remote atmosphere during both NH summer and NH winter. The ensemble spread increases from a factor of 40 in the NH source regions to a factor of 1000 in remote regions of the Southern Ocean. The evaluation of AeroCom-II models in the remote regions provides an extension of the previous evaluation with continental ground data by Tsigaridis et al. (2014). We note that the data from the AeroCom-II models were based on monthly mean values from a different simulated year than the ATom campaigns; however, the consistent model biases are strong enough that we would not expect our conclusions to change for a different modeled year.
- The results of the ATom model ensemble used in this work show a much better agreement with the OA observations in all regions and reduced model variability. However, some of the agreement is for the wrong reasons, as most models severely overestimate the contribution of POA and underestimate the contribution of SOA to total OA. Sensitivity simulations indicate that the POA overestimate in CESM could be due to an inadequate representation of primary aerosol removal by convective clouds, (additional convective removal per Yu et al. (2019) in CESM1-CARMA led to a better agreement with observations). Most models have insufficient production of SOA, and sensitivity studies indicate that a stronger production of SOA is needed to capture the measured concentrations. The photochemical ageing of POA which was not considered here (unlike for SOA) could also contribute to the model overestimation. The non-volatile POA treatment in models is consistent with the assumption of inert POA particles used to estimate POA from measurements, and cannot explain the

model bias. Indeed, sensitivity simulations with semi-volatile POA lead to a much larger model bias for OA in the upper troposphere and remote regions. The compensation between errors in POA and SOA in remote regions is however a recurring issue in OA modeling (de Gouw and Jimenez, 2009). For instance, it was found in the urban outflow regions such as Mexico City during MILAGRO 2006 field campaign (Fast et al., 2009; Hodzic et al., 2009); Paris during MEGAPOLI 2009 (Zhang et al., 2013); the Los Angeles area during CalNex-2010 (Baker et al., 2015; Woody et al., 2016); the NE US outflow during WINTER 2015 (Schroder et al., 2018; Shah et al., 2019).

- Additional errors in simulated OA concentrations can arise from the use of too low OA/OC ratios when model results (often calculated as OC) are converted to OA for comparison with measurements. We note that OA is the most atmospherically-relevant quantity, while OC is an operational quantity, partially a relic from a period in which only OC could be separately quantified (although also of some use for carbon budget studies). It should also be noted that most emission inventories still use OC as the primary variable, which is why the use of accurate OA/OC ratios is still key for all models. We show that the OA/OC ratio used in most models is too low compared to measured values that range mostly from 2.2 to 2.5, resulting in errors in OA mass of ~70% for AeroCom-II models and ~30% for current models that use organic carbon to track OA mass. Remote OA is thus highly oxidized and chemically processed. These results demonstrate that current global chemistry-climate models underestimate the degree of oxidation of OA in remote regions and need to consider further chemical ageing of OA, which could impact the calculations of its burden, and optical and hygroscopic properties.
- The results also show that in most models (except CESM2) the predicted OA contribution to the total submicron aerosol is underestimated relative to sulfate in the remote FT where OA and sulfate are the dominant submicron aerosols (important for climate). Accurate predictions of composition of submicron particles remains challenging in remote regions and should be the topic of future studies.

Key implications of our results are: (i) Model errors on the relative contribution of POA and SOA to OA reduce our confidence on the ability to simulate radiative forcing over time or OA health impacts; (ii) Model errors for the relative contributions of sulfate and organics to the submicron aerosol in the free troposphere could lead to errors in the predicted CCN or radiative forcing of aerosols as inorganics are more hygroscopic than OA; (iii) the OA

system seems to be more dynamic with a need for an enhanced removal of primary OA, and a stronger production of secondary OA in global models to provide a better agreement with observations.

Acknowledgements. The authors want to thank the ATom leadership team and the NASA logistics and flight crew for their contributions to the success of ATom. Authors acknowledge Dr. Rebecca Buchholz (NCAR) for providing the emissions used for the CESM2 simulations. The ATOM measurements and analyses were supported by NASA grants NNX15AH33A, NNX15AJ23G, and 80NSSC19K0124. AH was supported by the National Center for Atmospheric Research, which is operated by the University Corporation for Atmospheric Research on behalf of the National Science Foundation. JRP and JKK were supported by the US Department of Energy's Atmospheric System Research, an Office of Science, Office of Biological and Environmental Research program, under grant no. DE-SC0019000. This project has received support from the European Research Council under the European Union's Horizon 2020 research and innovation programme (grant agreement No. 819169), and from EPA STAR grant 83587701-0. This manuscript has not been reviewed by EPA, and no endorsement should be inferred. We would like to acknowledge high-performance computing support from Cheyenne provided by NCAR's Computational and Information Systems Laboratory. We thank C. Brock for the aerosol volume data, and D. Murphy for useful discussions. We thank the ATom leadership team, science team and the NASA DC-8 crew for their contributions to the success of the ATom mission.

Code/Data availability: Data can be obtained from the ATom website: https://doi.org/10.3334/ORNLDAAC/1581.

L2 Measurements from CU High-Resolution Aerosol Mass Spectrometer (HR-AMS) can be obtained from the ORNL DAAC, Oak Ridge, Tennessee, USA. https://doi.org/10.3334/ORNLDAAC/1716.

Author contribution: A. Hodzic, P. Campuzano-Jost and J.L. Jimenez performed the measurement / model comparisons, wrote and revised the manuscript. P. Campuzano-Jost, D.A. Day, B.N. Nault, J.C. Schroder, D.T. Sueper, and J. L. Jimenez performed and analyzed the AMS measurements. K.D. Froyd and G.P. Schill performed and analyzed the PALMS measurements. J.P. Schwarz and J.M. Katich performed the BC measurements. H. Bian, M. Chin, P.R. Colarco, B. Heinold, A. Hodzic, D.S. Jo, J.K.

Kodros, J.R. Pierce, E. Ray, J. Schacht, I. Tegen, S. Tilmes, K. Tsigaridis, and P. Yu provided model output. All authors provided comments on the manuscript.

References

Aiken, A.C., P.F. DeCarlo, J.H. Kroll, D.R. Worsnop, J.A. Huffman, K. Docherty, I.M. Ulbrich, C. Mohr, J.R. Kimmel, D. Sueper, Q. Zhang, Y. Sun, A. Trimborn, M. Northway, P.J. Ziemann, M.R. Canagaratna, T.B. Onasch, R. Alfarra, A.S.H. Prevot, J. Dommen, J. Duplissy, A. Metzger, U. Baltensperger, and J.L. Jimenez. O/C and OM/OC Ratios of Primary, Secondary, and Ambient Organic Aerosols with High Resolution Time-of-Flight Aerosol Mass Spectrometry Environmental Science & Technology, 42, 4478–4485, doi: 10.1021/es703009q, 2008.

Andreae, M. O.: Emission of trace gases and aerosols from biomass burning – An updated assessment, Atmos. Chem. Phys. Discuss., 1–27, doi:10.5194/acp-2019-303, 2019.

Bahreini, R., Ervens, B., Middlebrook, A. M., Warneke, C., de Gouw, J. A., DeCarlo, P. F., Jimenez, J. L., Brock, C. A., Neuman, J. A., Ryerson, T. B., Stark, H., Atlas, E., Brioude, J., Fried, A., Holloway, J. S., Peischl, J., Richter, D., Walega, J., Weibring, P., Wollny, A. G. and Fehsenfeld, F. C.: Organic aerosol formation in urban and industrial plumes near Houston and Dallas, Texas, J. Geophys. Res., 114, D00F16, doi:10.1029/2008JD011493, 2009.

Baker, K. R., Carlton, A. G., Kleindienst, T. E., Offenberg, J. H., Beaver, M. R., Gentner, D. R., Goldstein, A. H., Hayes, P. L., Jimenez, J. L., Gilman, J. B., de Gouw, J. A., Woody, M. C., Pye, H. O. T., Kelly, J. T., Lewandowski, M., Jaoui, M., Stevens, P. S., Brune, W. H., Lin, Y.-H., Rubitschun, C. L., and Surratt, J. D.: Gas and aerosol carbon in California: comparison of measurements and model predictions in Pasadena and Bakersfield, Atmos. Chem. Phys., 15, 5243-5258, https://doi.org/10.5194/acp-15-5243-2015, 2015.

Bey, I., Jacob, D. J., Yantosca, R. M., and Logan, J. A.: Global modeling of tropospheric chemistry with assimilated meteorology: model description and evaluation, J Geophys. Res., 106, 23073–23095, 2011.

Bian, H., Froyd, K., Murphy, D. M., Dibb, J., Chin, M., Colarco, P. R., Darmenov, A., da Silva, A., Kucsera, T. L., Schill, G., Yu, H., Bui, P., Dollner, M., Weinzierl, B., and Smirnov, A.: Observationally constrained analysis of sea salt aerosol in the marine atmosphere, Atmos. Chem. Phys. Discuss., https://doi.org/10.5194/acp-2019-18, 2019.

1112 Bian, H., Chin, M., Hauglustaine, D. A., Schulz, M., Myhre, G., Bauer, S. E., Lund, M. T.,
1113 Karydis, V. A., Kucsera, T. L., Pan, X., Pozzer, A., Skeie, R. B., Steenrod, S. D., Sudo, K.,
1114 Tsigaridis, K., Tsimpidi, A. P., and Tsyro, S. G.: Investigation of global nitrate from the
1115 AeroCom Phase III experiment, Atmos. Chem. Phys., 17, 12911-12940,
1116 https://doi.org/10.5194/acp-17-12911-2017, 2017.

1117 Boucher, O., D. Randall, P. Artaxo, C. Bretherton, G. Feingold, P. Forster, V.-M.
1118 Kerminen, Y. Kondo, H. Liao, U. Lohmann, P. Rasch, S.K. Satheesh, S. Sherwood, B.
1119 Stevens and X.Y. Zhang: Clouds and Aerosols. In: Climate Change 2013: The Physical
1120 Science Basis. Contribution of Working Group I to the Fifth Assessment Report of the
1121 Intergovernmental Panel on Climate Change [Stocker, T.F., D. Qin, G.-K. Plattner, M.
1122 Tignor, S.K. Allen, J. Boschung, A. Nauels, Y. Xia, V. Bex and P.M. Midgley (eds.)].
1123 Cambridge University Press, Cambridge, United Kingdom and New York, NY, USA, 2013.

1124 Bowman, K. P.: Large-scale isentropic mixing properties of the Antarctic polar vortex from
1125 analyzed winds. J. Geophys. Res., 98 (D12), 23 013–23 027, 1993.

1126 Brock, C. A., Wagner, N. L., Anderson, B. E., Attwood, A. R., Beyersdorf, A., Campuzano-
1127 Jost, P., Carlton, A. G., Day, D. A., Diskin, G. S., Gordon, T. D., Jimenez, J. L., Lack, D.
1128 A., Liao, J., Markovic, M. Z., Middlebrook, A. M., Ng, N. L., Perring, A. E., Richardson, M.
1129 S., Schwarz, J. P., Washenfelder, R. A., Welti, A., Xu, L., Ziemba, L. D., and Murphy, D.
1130 M.: Aerosol optical properties in the southeastern United States in summer – Part 1:
1131 Hygroscopic growth, Atmos. Chem. Phys., 16, 4987-5007, https://doi.org/10.5194/acp-16-
1132 4987-2016, 2016.

1133 Brock, C. A., Williamson, C., Kupc, A., Froyd, K. D., Erdesz, F., Wagner, N., Richardson,
1134 M., Schwarz, J. P., Gao, R.-S., Katich, J. M., Campuzano-Jost, P., Nault, B. A., Schroder,
1135 J. C., Jimenez, J. L., Weinzierl, B., Dollner, M., Bui, T. and Murphy, D. M.: Aerosol size
1136 distributions during the Atmospheric Tomography Mission (ATom): methods,
1137 uncertainties, and data products, Atmos. Meas. Tech., 12(6), 3081–3099,
1138 doi:10.5194/amt-12-3081-2019, 2019.

1139 Canagaratna, M. R., Jayne, J. T., Jimenez, J. L., Allan, J. D., Alfarra, M. R., Zhang, Q.,
1140 Onasch, T. B., Drewnick, F., Coe, H., Middlebrook, A. M., Delia, A., Williams, L. R.,
1141 Trimborn, A. M., Northway, M. J., DeCarlo, P. F., Kolb, C. E., Davidovits, P., and Worsnop,
1142 D. R.: Chemical and microphysical characterization of ambient aerosols with the Aerodyne

1143 Aerosol Mass Spectrometer, Mass Spectrom. Rev., 26, 185–222,
1144 https://doi.org/10.1002/mas.20115, 2007.

1145 Canagaratna, M. R., Jimenez, J. L., Kroll, J. H., Chen, Q., Kessler, S. H., Massoli, P.,
1146 Hildebrandt Ruiz, L., Fortner, E., Williams, L. R., Wilson, K. R., Surratt, J. D., Donahue, N.
1147 M., Jayne, J. T., and Worsnop, D. R.: Elemental ratio measurements of organic
1148 compounds using aerosol mass spectrometry: characterization, improved calibration, and
1149 implications, Atmos. Chem. Phys., 15, 253-272, https://doi.org/10.5194/acp-15-253-2015,
1150 2015.

1151 Carslaw, K. S., Lee, L. a, Reddington, C. L., Pringle, K. J., Rap, A., Forster, P. M., Mann,
1152 G. W., Spracklen, D. V, Woodhouse, M. T., Regayre, L. a and Pierce, J. R.: Large
1153 contribution of natural aerosols to uncertainty in indirect forcing., Nature, 503(7474), 67–
1154 71, doi:10.1038/nature12674, 2013.

1155 Colarco, P., da Silva, A., Chin, M., and Diehl, T.: Online simulations of global aerosol
1156 distributions in the NASA GEOS-4 model and comparisons to satellite and ground based
1157 aerosol optical depth, J. Geophys. Res., 115, D14207, doi:10.1029/2009JD012820, 2010.

1158 Croft, B., Lohmann, U., Martin, R. V., Stier, P., Wurzler, S., Feichter, J., Hoose, C.,
1159 Heikkilä, U., van Donkelaar, A., and Ferrachat, S.: Influences of in-cloud aerosol
1160 scavenging parameterizations on aerosol concentrations and wet deposition in ECHAM5-
1161 HAM, Atmos. Chem. Phys., 10, 1511–1543, https://doi.org/10.5194/acp-10-1511-2010,
1162 2010.

1163 Cubison, M. J., Ortega, A. M., Hayes, P. L., Farmer, D. K., Day, D., Lechner, M. J., Brune,
1164 W. H., Apel, E., Diskin, G. S., Fisher, J. A., Fuelberg, H. E., Hecobian, A., Knapp, D. J.,
1165 Mikoviny, T., Riemer, D., Sachse, G. W., Sessions, W., Weber, R. J., Weinheimer, A. J.,
1166 Wisthaler, A., and Jimenez, J. L.: Effects of aging on organic aerosol from open biomass
1167 burning smoke in aircraft and laboratory studies, Atmos. Chem. Phys., 11, 12049-12064,
1168 https://doi.org/10.5194/acp-11-12049-2011, 2011.

1169 DeCarlo, P., Slowik, J., Worsnop, D., Davidovits, P., Jimenez, J., Stainken, K., Williams,
1170 L., Jayne, J., Kolb, C. and Rudich, Y.: Particle Morphology and Density Characterization
1171 by Combined Mobility and Aerodynamic Diameter Measurements. Part 1: Theory, Aerosol
1172 Sci. Technol., 38(12), 1185–1205, doi:10.1080/027868290903907, 2004.

1173 DeCarlo, P. F., Kimmel, J. R., Trimborn, A., Northway, M. J., Jayne, J. T., Aiken, A. C.,
1174 Gonin, M., Fuhrer, K., Horvath, T., Docherty, K. S., Worsnop, D. R., and Jimenez, J. L.:

1175 Field-Deployable, High-Resolution, Time-of-Flight Aerosol Mass Spectrometer, Anal.
1176 Chem., 78, 8281–8289, https://doi.org/10.1021/ac061249n, 2006.

1177 de Gouw, J., and J.L. Jimenez. Organic Aerosols in the Earth's Atmosphere.
1178 Environmental Science & Technology, 43, 7614–7618, 2009. DOI: 10.1021/es9006004

1179 Dentener, F., Kinne, S., Bond, T., Boucher, O., Cofala, J., Generoso, S., Ginoux, P., Gong,
1180 S., Hoelzemann, J. J., Ito, A., Marelli, L., Penner, J. E., Putaud, J.-P., Textor, C., Schulz,
1181 M., van der Werf, G. R., and Wilson, J.: Emissions of primary aerosol and precursor gases
1182 in the years 2000 and 1750 prescribed data-sets for AeroCom, Atmospheric Chemistry
1183 and Physics, 6, 4321–4344, https://doi.org/10.5194/acp- 6-4321-2006,
1184 https://www.atmos-chem-phys.net/6/4321/2006/, 2006.

1185 Ditas, J., Ma, N., Zhang, Y., Assmann, D., et al.: Strong impact of wildfires on the
1186 abundance and aging of black carbon in the lowermost stratosphere, Proc. Natl. Acad.
1187 Sci., 811595-11603, doi:10.1073/pnas.1806868115, 2018.

1188 Drewnick, F., Hings, S. S., Alfarra, M. R., Prevot, A. S. H. and Borrmann, S.: Aerosol
1189 quantification with the Aerodyne Aerosol Mass Spectrometer: detection limits and ionizer
1190 background effects, Atmos. Meas. Tech., 2(1), 33–46, 2009.

1191 Emmons, L. K., Orlando, J. J., Tyndall, G., Schwantes, R. H., Kinnison, D. E., Marsh, D.
1192 R., Mills, M. J., Tilmes, S., and Lamarque, J.-F.: The MOZART Chemistry Mechanism in
1193 the Community Earth System Model version 2 (CESM2), to be Submitted to J. Adv.
1194 Modeling Earth Systems, 2019.

1195 Farmer, D.K., A. Matsunaga, K.S. Docherty, J.D. Surratt, J.H. Seinfeld, P.J. Ziemann, and
1196 J.L. Jimenez. Response of an Aerosol Mass Spectrometer to Organonitrates and
1197 Organosulfates and implications for Atmospheric Chemistry. Proceedings of the National
1198 Academy of Sciences of the USA, 107, 6670-6675, doi: 10.1073/pnas.0912340107, 2010.

1199 Fast, J., Aiken, A. C., Allan, J., Alexander, L., Campos, T., Canagaratna, M. R., Chapman,
1200 E., DeCarlo, P. F., de Foy, B., Gaffney, J., de Gouw, J., Doran, J. C., Emmons, L., Hodzic,
1201 A., Herndon, S. C., Huey, G., Jayne, J. T., Jimenez, J. L., Kleinman, L., Kuster, W., Marley,
1202 N., Russell, L., Ochoa, C., Onasch, T. B., Pekour, M., Song, C., Ulbrich, I. M., Warneke,
1203 C., Welsh-Bon, D., Wiedinmyer, C., Worsnop, D. R., Yu, X.-Y., and Zaveri, R.: Evaluating
1204 simulated primary anthropogenic and biomass burning organic aerosols during
1205 MILAGRO: implications for assessing treatments of secondary organic aerosols, Atmos.
1206 Chem. Phys., 9, 6191-6215, https://doi.org/10.5194/acp-9-6191-2009, 2009.

1207 Feng, L., Smith, S. J., Braun, C., Crippa, M., Gidden, M. J., Hoesly, R., Klimont, Z., van
1208 Marle, M., van den Berg, M., and van der Werf, G. R.: Gridded Emissions for CMIP6,
1209 Geosci. Model Dev. Discuss., https://doi.org/10.5194/gmd-2019-195, in review, 2019.

1210 Flamant, C., Knippertz, P., Fink, A. H., Akpo, A., Brooks, B., Chiu, C. J., Coe, H., Danuor,
1211 S., Evans, M., Jegede, O., Kalthoff, N., Konaré, A., Liousse, C., Lohou, F., Mari, C.,
1212 Schlager, H., Schwarzenboeck, A., Adler, B., Amekudzi, L., Aryee, J., Ayoola, M.,
1213 Batenburg, A. M., Bessardon, G., Borrmann, S., Brito, J., Bower, K., Burnet, F., Catoire,
1214 V., Colomb, A., Den- jean, C., Fosu-Amankwah, K., Hill, P. G., Lee, J., Lothon, M.,
1215 Maranan, M., Marsham, J., Meynadier, R., Ngamini, J.-B., Rosenberg, P., Sauer, D.,
1216 Smith, V., Stratmann, G., Taylor, J. W., Voigt, C., and Yoboué, V.: The Dynamics-Aerosol-
1217 Chemistry- Cloud Interactions in West Africa field campaign: Overview and research
1218 highlights, B. Am. Meteorol. Soc., 99, 83–104, https://doi.org/10.1175/BAMS-D-16-
1219 0256.1, 2018.

1220 Forrister, H., Liu, J., Scheuer, E., Dibb, J., Ziemba, L., Thornhill, K. L., Anderson, B.,
1221 Diskin, G., Perring, A. E., Schwarz, J. P., Campuzano-Jost, P., Day, D. A., Palm, B. B.,
1222 Jimenez, J. L., Nenes, A. and Weber, R. J.: Evolution of brown carbon in wildfire plumes,
1223 Geophys. Res. Lett., 42(11), doi:10.1002/2015GL063897, 2015.

1224 Fountoukis, C. and Nenes, A.: ISORROPIA II : a computationally efficient thermodynamic
1225 equilibrium model for K+-Ca2+-Mg2+-Na+-SO42--NO3--Cl--H2O aerosols, Atmos. Chem.
1226 Phys., 7, 4639–4659, 2007.

1227 Froyd, K. D., Murphy, D. M., Brock, C. A., Campuzano-Jost, P., Dibb, J. E., Jimenez, J.-
1228 L., Kupc, A., Middlebrook, A. M., Schill, G. P., Thornhill, K. L., Williamson, C. J., Wilson,
1229 J. C., and Ziemba, L. D.: A new method to quantify mineral dust and other aerosol species
1230 from aircraft platforms using single particle mass spectrometry, Atmos. Meas. Tech.
1231 Discuss., https://doi.org/10.5194/amt-2019-165, in review, 2019.

1232 George, I. J. and Abbatt, J. P. D.: Heterogeneous oxidation of atmospheric aerosol
1233 particles by gas-phase radicals, Nature Chemistry, 2, 713–722, 2010.

1234 Gettelman, A., Mills, M. J., Kinnison, D. e., Garcia, R. R., Smith, A. K., Marsh, D. R.,
1235 Tilmes, S., Vitt, F., Bardeen, C. G., McInerny, J., Liu, H.-L., Solomon, S. C., Polvani, L.
1236 M., Emmons, L. K., Lamarque, J.-F., Richter, J. H., Glanville, A. S., Bacmeister, J. T.,
1237 Phillips, A. S., Neale, R. B., Simpson, I. R., DuVivier, A. K., Hodzic, A., Randel, W. J.: The

1238 Whole Atmosphere Community Climate Model Version 6 (WACCM6), J. of Geophys. Res.,
1239 in review, 2019.

1240 Gerber, H. E.: Relative-humidity parameterization of the Navy Aerosol Model (NAM),
1241 Tech. Rep. NRL Report 8956, Naval Research Laboratory, 1985.

1242 Giglio, L., Randerson, J. T. and Werf, G. R.: Analysis of daily, monthly, and annual burned
1243 area using the fourth-generation global fire emissions database (GFED4), J. Geophys.
1244 Res. Biogeosciences, 118, 317–328, 2013.

1245 Guenther, A. B., Jiang, X., Heald, C. L., Sakulyanontvittaya, T., Duhl, T., Emmons, L. K.,
1246 and Wang, X.: The Model of Emissions of Gases and Aerosols from Nature version 2.1
1247 (MEGAN2.1): an extended and updated framework for modeling biogenic emissions,
1248 Geosci. Model Dev., 5, 1471–1492, https://doi.org/10.5194/gmd-5-1471-2012,
1249 https://www.geosci-model-dev.net/5/1471/2012/, 2012.

1250 Hayes, P. L., Carlton, A. G., Baker, K. R., Ahmadov, R., Washenfelder, R. A., Alvarez, S.,
1251 Rappenglück, B., Gilman, J. B., Kuster, W. C., de Gouw, J. A., Zotter, P., Prévôt, A. S. H.,
1252 Szidat, S., Kleindienst, T. E., Offenberg, J. H., Ma, P. K., and Jimenez, J. L.: Modeling the
1253 formation and aging of secondary organic aerosols in Los Angeles during CalNex 2010,
1254 Atmos. Chem. Phys., 15, 5773-5801, https://doi.org/10.5194/acp-15-5773-2015, 2015.

1255 Hallquist, M., Wenger, J. C., Baltensperger, U., Rudich, Y., Simpson, D., Claeys, M.,
1256 Dommen, J., Donahue, N. M., George, C., Goldstein, A. H., Hamilton, J. F., Herrmann, H.,
1257 Hoffmann, T., Iinuma, Y., Jang, M., Jenkin, M. E., Jimenez, J. L., Kiendler-Scharr, A.,
1258 Maenhaut, W., McFiggans, G., Mentel, Th. F., Monod, A., Prévôt, A. S. H., Seinfeld, J. H.,
1259 Surratt, J. D., Szmigielski, R., and Wildt, J.: The formation, properties and impact of
1260 secondary organic aerosol: current and emerging issues, Atmos. Chem. Phys., 9, 5155-
1261 5236, https://doi.org/10.5194/acp-9-5155-2009, 2009.

1262 Heald, C. L., Coe, H., Jimenez, J. L., Weber, R. J., Bahreini, R., Middlebrook, A. M.,
1263 Russell, L. M., Jolleys, M., Fu, T.-M., Al- lan, J. D., Bower, K. N., Capes, G., Crosier, J.,
1264 Morgan, W. T., Robinson, N. H., Williams, P. I., Cubison, M. J., DeCarlo, P. F., and Dunlea,
1265 E. J.: Exploring the vertical profile of atmospheric organic aerosol: comparing 17 aircraft
1266 field campaigns with a global model, Atmos. Chem. Phys., 11, 12673–12696,
1267 doi:10.5194/acp-11-12673-2011, 2011.

1268 Hodshire, A. L., Campuzano-Jost, P., Kodros, J. K., Croft, B., Nault, B. A., Schroder, J.
1269 C., Jimenez, J. L. and Pierce, J. R.: The potential role of methanesulfonic acid (MSA) in

aerosol formation and growth and the associated radiative forcings, Atmos. Chem. Phys., 19(5), 3137–3160, doi:10.5194/acp-19-3137-2019, 2019a.

Hodshire, A., A. Akherati, M. Alvarado, B. Brown-Steiner, S. Jathar, J.L. Jimenez, S. Kreidenweis, C. Lonsdale, T. Onasch, A. Ortega, J. Pierce. Aging Effects on Biomass Burning Aerosol Mass and Composition: A Critical Review of Field and Laboratory Studies. Environ. Sci. Technol., submitted, 2019b.

Hodzic, A., Jimenez, J. L., Madronich, S., Aiken, A. C., Bessagnet, B., Curci, G., Fast, J., Lamarque, J.-F., Onasch, T. B., Roux, G., Schauer, J. J., Stone, E. A., and Ulbrich, I. M.: Modeling organic aerosols during MILAGRO: importance of biogenic secondary organic aerosols, Atmos. Chem. Phys., 9, 6949-6981, https://doi.org/10.5194/acp-9-6949-2009, 2009.

Hodzic, A., Aumont, B., Knote, C., Lee-Taylor, J., Madronich, S., and Tyndall, G.: Volatility dependence of Henry's law constants of condensable organics: Application to estimate depositional loss of secondary organic aerosols, Geophys. Res. Lett., 41, 4795–4804, doi:10.1002/2014GL060649, 2014.

Hodzic, A., Madronich, S., Kasibhatla, P. S., Tyndall, G., Aumont, B., Jimenez, J. L., Lee-Taylor, J., and Orlando, J.: Organic photolysis reactions in tropospheric aerosols: effect on secondary organic aerosol formation and lifetime, Atmos. Chem. Phys., 15, 9253-9269, https://doi.org/10.5194/acp-15-9253-2015, 2015.

Hodzic, A., Kasibhatla, P. S., Jo, D. S., Cappa, C. D., Jimenez, J. L., Madronich, S., and Park, R. J.: Rethinking the global secondary organic aerosol (SOA) budget: stronger production, faster removal, shorter lifetime, Atmos. Chem. Phys., 16, 7917-7941, https://doi.org/10.5194/acp-16-7917-2016, 2016.

Hoesly, R. M., Smith, S. J., Feng, L., Klimont, Z., Janssens-Maenhout, G., Pitkanen, T., Seibert, J. J., Vu, L., Andres, R. J., Bolt, R. M., Bond, T. C., Dawidowski, L., Kholod, N., Kurokawa, J.-I., Li, M., Liu, L., Lu, Z., Moura, M. C. P., O'Rourke, P. R., and Zhang, Q.: Historical (1750–2014) anthropogenic emissions of reactive gases and aerosols from the Community Emissions Data System (CEDS), Geosci. Model Dev., 11, 369–408, https://doi.org/10.5194/gmd-11-369-2018, 2018.

Huang, K., Fu, J. S., Prikhodko, V. Y., Storey, J. M., Romanov, A., Hodson, E. L., Cresko, J., Morozova, I., Ignatieva, Y., and Cabaniss, J.: Russian anthropogenic black carbon:

1301 Emission reconstruction and Arctic black carbon simulation, J. Geophys. Res. Atmos.,
1302 120, 11,306– 11,333, doi:10.1002/2015JD023358, 2015.

1303 Hudson, P. K., Murphy, D. M., Cziczo, D. J., Thomson, D. S., de Gouw, J. A., Warneke,
1304 C., Holloway, J., Jost, H. J. and Hübler, G.: Biomass-burning particle measurements:
1305 Characteristics composition and chemical processing, J. Geophys. Res. D Atmos.,
1306 109(23), 1–11, doi:10.1029/2003JD004398, 2004.

1307 Janssens-Maenhout, G., Crippa, M., Guizzardi, D., Dentener, F., Muntean, M., Pouliot,
1308 G., Keating, T., Zhang, Q., Kurokawa, J., Wankmüller, R., Denier van der Gon, H.,
1309 Kuenen, J. J. P., Klimont, Z., Frost, G., Darras, S., Koffi, B., and Li, M.: HTAP_v2.2: a
1310 mosaic of regional and global emission grid maps for 2008 and 2010 to study hemispheric
1311 transport of air pollution, Atmos. Chem. Phys., 15, 11411–11432,
1312 https://doi.org/10.5194/acp-15-11411-2015, 2015.

1313 Jimenez, J. L., Canagaratna, M. R., Donahue, N. M., Prevot, a. S. H., Zhang, Q., Kroll, J.
1314 H., DeCarlo, P. F., Allan, J. D., Coe, H., Ng, N. L., Aiken, a. C., Docherty, K. S., Ulbrich, I.
1315 M., Grieshop, A. P., Robinson, a. L., Duplissy, J., Smith, J. D., Wilson, K. R., Lanz, V. a.,
1316 Hueglin, C., Sun, Y. L., Tian, J., Laaksonen, A., Raatikainen, T., Rautiainen, J.,
1317 Vaattovaara, P., Ehn, M., Kulmala, M., Tomlinson, J. M., Collins, D. R., Cubison, M. J.,
1318 Dunlea, E. J., Huffman, J. A., Onasch, T. B., Alfarra, M. R., Williams, P. I., Bower, K.,
1319 Kondo, Y., Schneider, J., Drewnick, F., Borrmann, S., Weimer, S., Demerjian, K., Salcedo,
1320 D., Cottrell, L., Griffin, R., Takami, A., Miyoshi, T., Hatakeyama, S., Shimono, A., Sun, J.
1321 Y., Zhang, Y. M., Dzepina, K., Kimmel, J. R., Sueper, D., Jayne, J. T., Herndon, S. C.,
1322 Trimborn, a. M., Williams, L. R., Wood, E. C., Middlebrook, A. M., Kolb, C. E.,
1323 Baltensperger, U., Worsnop, D. R., Worsnop, D. R., Dunlea, J., Huffman, J. A., Onasch,
1324 T. B., Alfarra, M. R., Williams, P. I., Bower, K., Kondo, Y., Schneider, J., Drewnick, F.,
1325 Borrmann, S., Weimer, S., Demerjian, K., Salcedo, D., Cottrell, L., Griffin, R., Takami, A.,
1326 Miyoshi, T., Hatakeyama, S., Shimono, A., Sun, J. Y., Zhang, Y. M., Dzepina, K., Kimmel,
1327 J. R., Sueper, D., Jayne, J. T., Herndon, S. C., Trimborn, a. M., Williams, L. R., Wood, E.
1328 C., Middlebrook, A. M., Kolb, C. E., Baltensperger, U., Worsnop, D. R., Dunlea, E. J., et
1329 al.: Evolution of Organic Aerosols in the Atmosphere, Science 80., 326(5959), 1525–1529,
1330 doi:10.1126/science.1180353, 2009.

1331 Jimenez, J.L., P. Campuzano-Jost, D.A. Day, B.A. Nault, D.J. Price, and J.C. Schroder:
1332 ATom: L2 Measurements from CU High-Resolution Aerosol Mass Spectrometer (HR-

AMS). ORNL DAAC, Oak Ridge, Tennessee, USA. https://doi.org/10.3334/ORNLDAAC/1716, 2019a.

Jimenez, J.L., et al.: Evaluating the Consistency of All Submicron Aerosol Mass Measurements (Total and Speciated) in the Atmospheric Tomography Mission (ATom), Abstract A31A-08, presented at 2019 Fall Meeting, AGU, San Francisco, CA, 9-13 Dec., 2019b.

Jolleys, M. D., Coe, H., McFiggans, G., Taylor, J. W., O'Shea, S. J., Le Breton, M., Bauguitte, S. J.-B., Moller, S., Di Carlo, P., Aruffo, E., Palmer, P. I., Lee, J. D., Percival, C. J. and Gallagher, M. W.: Properties and evolution of biomass burning organic aerosol from Canadian boreal forest fires, Atmos. Chem. Phys., 15(6), 3077–3095, doi:10.5194/acp-15-3077-2015, 2015.

Kaiser, J. W., Heil, A., Andreae, M. O., Benedetti, A., Chubarova, N., Jones, L., Morcrette, J.-J., Razinger, M., Schultz, M. G., Suttie, M., and van der Werf, G. R.: Biomass burning emissions estimated with a global fire assimilation system based on observed fire radiative power, Biogeosciences, 9, 527–554, https://doi.org/10.5194/bg-9-527-2012, https://www.biogeosciences.net/9/527/2012/, 2012.

Kanakidou, M., Seinfeld, J. H., Pandis, S. N., Barnes, I., Dentener, F. J., Facchini, M. C., Van Dingenen, R., Ervens, B., Nenes, A., Nielsen, C. J., Swietlicki, E., Putaud, J. P., Balkanski, Y., Fuzzi, S., Horth, J., Moortgat, G. K., Winterhalter, R., Myhre, C. E. L., Tsigaridis, K., Vignati, E., Stephanou, E. G., and Wilson, J.: Organic aerosol and global climate modelling: a review, Atmos. Chem. Phys., 5, 1053-1123, https://doi.org/10.5194/acp-5-1053-2005, 2005.

Katich, J. M., Samset, B. H., Paul Bui, T., Dollner, M., Froyd, K.D., Campuzano-Jost, P., Nault, B. A., Schroder, J. C., Weinzierl, B., Schwarz, J. P.: Strong Contrast in Remote Black Carbon Aerosol Loadings Between the Atlantic and Pacific Basins, J. Geophys. Res. Atmos., 123 (23), pages 13,386-13,395, https://doi.org/10.1029/2018JD029206, 2018.

Kim, M. J., G. A. Novak, M. C. Zoerb,M. Yang, B. W. Blomquist, B. J. Huebert, C. D. Cappa, and T. H. Bertram: Air-Sea exchange of biogenic volatile organic compounds and the impact on aerosol particle size distributions, Geophys. Res. Lett.,44, 3887–3896, doi:10.1002/2017GL072975, 2017.

1363 Klimont, Z., K. Kupiainen, C. Heyes, P. Purohit, J. Cofala, P. Rafaj, J. Borken-Kleefeld,
1364 and W. Schöpp,: Global anthropogenic emissions of particulate matter including black
1365 carbon, Atmos. Chem. Phys., 17(14), 8681-8723, doi: 10.5194/acp-17-8681-2017, 2017.

1366 Kodros, J. K., Cucinotta, R., Ridley, D. A., Wiedinmyer, C., and Pierce, J. R.: The aerosol
1367 radiative effects of uncontrolled combustion of domestic waste, Atmos. Chem. Phys., 16,
1368 6771-6784, https://doi.org/10.5194/acp-16-6771-2016, 2016.

1369 Krechmer, J.E., D. Pagonis, P.J. Ziemann, and J.L. Jimenez. Quantification of gas-wall
1370 partitioning in Teflon environmental chambers using rapid bursts of low-volatility oxidized
1371 species generated in-situ. Environmental Science and Technology, 50, 5757–5765,
1372 doi:10.1021/acs.est.6b00606, 2016.

1373 Kroll, J. H., Donahue, N. M., Jimenez, J. L., Kessler, S. H., Canagaratna, M. R., Wilson,
1374 K. R., Altieri, K. E., Mazzoleni, L. R., Wozniak, A. S., Bluhm, H., Mysak, E. R., Smith, J.
1375 D., Kolb, C. E. and Worsnop, D. R.: Carbon oxidation state as a metric for describing the
1376 chemistry of atmospheric organic aerosol., Nat. Chem., 3(2), 133–9,
1377 doi:10.1038/nchem.948, 2011.

1378 Laskin, A., Laskin, J., and Nizkorodov, S.: Chemistry of Atmospheric Brown Carbon,
1379 Chem. Rev. 2015, 115, 10, 4335-4382, 2015.

1380 Lee, A. K. Y., Willis, M. D., Healy, R. M., Onasch, T. B., and Abbatt, J. P. D.: Mixing state
1381 of carbonaceous aerosol in an urban environment: single particle characterization using
1382 the soot particle aerosol mass spectrometer (SP-AMS), Atmos. Chem. Phys., 15, 1823-
1383 1841, https://doi.org/10.5194/acp-15-1823-2015, 2015.

1384 Liao, J., K.D. Froyd, D.M. Murphy, F.N. Keutsch, G. Yu, P.O.Wennberg, J.St. Clair, J.D.
1385 Crounse, A. Wisthaler, T. Mikoviny, T.B. Ryerson, I.B. Pollack, J. Peischl, J.L. Jimenez,
1386 P. Campuzano Jost, D.A. Day, B.E. Anderson, L.D. Ziemba, D.R. Blake, S. Meinardi, G.
1387 Diskin. Airborne organosulfates measurements over the continental US. Journal of
1388 Geophysical Research-Atmospheres, 120, 2990–3005, doi:10.1002/2014JD022378,
1389 2015.

1390 Liu, H. Y., D. J. Jacob, I. Bey, and R. M. Yantosca: Constraints from Pb-210 and Be-7 on
1391 wet deposition and transport in a global three-dimensional chemical tracer model driven
1392 by assimilated meteorological fields, J. Geophys. Res., 106(D11), 12,109–12,128, 2001.

1393 Liu, X., Easter, R. C., Ghan, S. J., Zaveri, R., Rasch, P., Shi, X., Lamarque, J.-F.,
1394 Gettelman, A., Morrison, H., Vitt, F., Conley, A., Park, S., Neale, R., Hannay, C., Ekman,
1395 A. M. L., Hess, P., Mahowald, N., Collins, W., Iacono, M. J., Bretherton, C. S., Flanner, M.
1396 G., and Mitchell, D.: Toward a minimal representation of aerosols in climate models:
1397 description and evaluation in the Community Atmosphere Model CAM5, Geosci. Model
1398 Dev., 5, 709-739, https://doi.org/10.5194/gmd-5-709-2012, 2012.

1399 Marais, E. A., Jacob, D. J., Jimenez, J. L., Campuzano-Jost, P., Day, D. A., Hu, W.,
1400 Krechmer, J., Zhu, L., Kim, P. S., Miller, C. C., Fisher, J. A., Travis, K., Yu, K., Hanisco, T.
1401 F., Wolfe, G. M., Arkinson, H. L., Pye, H. O. T., Froyd, K. D., Liao, J., and McNeill, V. F.:
1402 Aqueous-phase mechanism for secondary organic aerosol formation from isoprene:
1403 application to the southeast United States and co-benefit of SO2 emission controls,
1404 Atmos. Chem. Phys., 16, 1603-1618, https://doi.org/10.5194/acp-16-1603-2016, 2016.

1405 Myhre, G., Samset, B. H., Schulz, M., Balkanski, Y., Bauer, S., Berntsen, T. K., Bian, H.,
1406 Bellouin, N., Chin, M., Diehl, T., Easter, R. C., Feichter, J., Ghan, S. J., Hauglustaine, D.,
1407 Iversen, T., Kinne, S., Kirkevåg, A., Lamarque, J.-F., Lin, G., Liu, X., Lund, M. T., Luo, G.,
1408 Ma, X., van Noije, T., Penner, J. E., Rasch, P. J., Ruiz, A., Seland, Ø., Skeie, R. B., Stier,
1409 P., Takemura, T., Tsigaridis, K., Wang, P., Wang, Z., Xu, L., Yu, H., Yu, F., Yoon, J.-H.,
1410 Zhang, K., Zhang, H., and Zhou, C.: Radiative forcing of the direct aerosol effect from
1411 AeroCom Phase II simulations, Atmos. Chem. Phys., 13, 1853-1877,
1412 https://doi.org/10.5194/acp-13-1853-2013, 2013.

1413 Mauderly, J. L., & Chow, J. C: Health Effects of Organic Aerosols, Inhalation Toxicology,
1414 20:3, 257-288, DOI: 10.1080/08958370701866008, 2008.

1415 Middlebrook, A. M., Murphy, D. M. and Thomson, D. S.: Observations of organic material
1416 in individual marine particles at Cape Grim during the First Aerosol Characterization
1417 Experiment (ACE 1), J. Geophys. Res. Atmos., 103(D13), 16475–16483,
1418 doi:10.1029/97JD03719, 1998.

1419 Murphy, D. M., Froyd, K. D., Bian, H., Brock, C. A., Dibb, J. E., DiGangi, J. P., Diskin, G.,
1420 Dollner, M., Kupc, A., Scheuer, E. M., Schill, G. P., Weinzierl, B., Williamson, C. J., and
1421 Yu, P.: The distribution of sea-salt aerosol in the global troposphere, Atmos. Chem. Phys.,
1422 19, 4093-4104, https://doi.org/10.5194/acp-19-4093-2019, 2019.

1423 Nault, B. A., Campuzano-Jost, P., Day, D. A., Schroder, J. C., Anderson, B., Beyersdorf,
1424 A. J., Blake, D. R., Brune, W. H., Choi, Y., Corr, C. A., de Gouw, J. A., Dibb, J., DiGangi,

J. P., Diskin, G. S., Fried, A., Huey, L. G., Kim, M. J., Knote, C. J., Lamb, K. D., Lee, T., Park, T., Pusede, S. E., Scheuer, E., Thornhill, K. L., Woo, J.-H., and Jimenez, J. L.: Secondary organic aerosol production from local emissions dominates the organic aerosol budget over Seoul, South Korea, during KORUS-AQ, Atmos. Chem. Phys., 18, 17769-17800, https://doi.org/10.5194/acp-18-17769-2018, 2018.

Ovadnevaite, J., Ceburnis, D., Canagaratna, M., Berresheim, H., Bialek, J., Martucci, G., Worsnop, D. R. and O'Dowd, C.: On the effect of wind speed on submicron sea salt mass concentrations and source fluxes, J. Geophys. Res. Atmos., 117(D16), 1–11, doi:10.1029/2011JD017379, 2012.

Pai, S. J., Heald, C. L., Pierce, J. R., Farina, S. C., Marais, E. A., Jimenez, J. L., Campuzano-Jost, P., Nault, B. A., Middlebrook, A. M., Coe, H., Shilling, J. E., Bahreini, R., Dingle, J. H., and Vu, K.: An evaluation of global organic aerosol schemes using airborne observations, Atmos. Chem. Phys. Discuss., https://doi.org/10.5194/acp-2019-331, in press, 2020.

Palm, B. B., de Sá, S. S., Day, D. A., Campuzano-Jost, P., Hu, W., Seco, R., Sjostedt, S. J., Park, J.-H., Guenther, A. B., Kim, S., Brito, J., Wurm, F., Artaxo, P., Thalman, R., Wang, J., Yee, L. D., Wernis, R., Isaacman-VanWertz, G., Goldstein, A. H., Liu, Y., Springston, S. R., Souza, R., Newburn, M. K., Alexander, M. L., Martin, S. T., and Jimenez, J. L.: Secondary organic aerosol formation from ambient air in an oxidation flow reactor in central Amazonia, Atmos. Chem. Phys., 18, 467–493, https://doi.org/10.5194/acp-18-467-2018, 2018.

Petters, M. D., Prenni, A. J., Kreidenweis, S. M., DeMott, P. J., Matsunaga, A., Lim, Y. B., and Ziemann, P. J. Chemical aging and the hydrophobic-to-hydrophilic conversion of carbonaceous aerosol, Geophys. Res. Lett., 33, L24806, doi:10.1029/2006GL027249, 2006.

Pye, H. O. T., Chan, A. W. H., Barkley, M. P., and Seinfeld, J. H.: Global modeling of organic aerosol: The importance of reactive nitrogen (NOx and NO_3), Atmos. Chem. Phys., 10, 11,261–11,276, doi:10.5194/acp-10-11261-2010, 2010.

Robinson, A. L., Donahue, N. M., Shrivastava, M. K., Weitkamp, E. A., Sage, A. M., Grieshop, A. P., Lane, T. E., Pandis, S. N., and Pierce, J. R.: Rethinking organic aerosols: Semivolatile emissions and photochemical aging, Science, 315, 1259–1262, 2007.

1456 Schroder, J. C., Campuzano-Jost, P., Day, D. A., Shah, V., Larson, K., Sommers, J. M.,
1457 Sullivan, A. P., Campos, T., Reeves, J. M., Hills, A., Hornbrook, R. S., Blake, N. J.,
1458 Scheuer, E., Guo, H., Fibiger, D. L., McDuffie, E. E., Hayes, P. L., Weber, R. J., Dibb, J.
1459 E., Apel, E. C., Jaeglé, L., Brown, S. S., Thornton, J. A. and Jimenez, J. L.: Sources and
1460 Secondary Production of Organic Aerosols in the Northeastern United States during
1461 WINTER, J. Geophys. Res. Atmos., 123(14), 7771–7796, doi:10.1029/2018JD028475,
1462 2018.

1463 Schacht, J., Heinold, B., Quaas, J., Backman, J., Cherian, R., Ehrlich, A., Herber, A.,
1464 Huang, W. T. K., Kondo, Y. Massling, A, Sinha, P.R., Weinzierl, B. Zanatta, M., and Tegen,
1465 I.: The importance of the representation of air pollution emissions for the modeled
1466 distribution and radiative effects of black carbon in the Arctic, Atmos. Chem. Phys.
1467 Discuss., 2019, 1-39, doi: 10.5194/acp-2019-71, 2019.

1468 Schulz, M., Chin, M., and Kinne, S.: The aerosol model comparison project, AeroCom,
1469 phase II: clearing up diversity, IGAC newsletter, No. 41, 2–11, 2009.

1470 Scott, C. E., Rap, A., Spracklen, D. V., Forster, P. M., Carslaw, K. S., Mann, G. W., Pringle,
1471 K. J., Kivekäs, N., Kulmala, M., Lihavainen, H., and Tunved, P.: The direct and indirect
1472 radiative effects of biogenic secondary organic aerosol, Atmos. Chem. Phys., 14, 447-
1473 470, https://doi.org/10.5194/acp-14-447-2014, 2014.

1474 Shah, V., Jaeglé, L., Jimenez, J. L., Schroder, J. C., Campuzano-Jost, P., Campos, T. L.,
1475 et al.: Widespread pollution from secondary sources of organic aerosols during winter in
1476 the Northeastern United States. Geophysical Research Letters, 46, 2974– 2983.
1477 https://doi.org/10.1029/2018GL081530, 2019.

1478 Shiraiwa, M., Ueda, K., Pozzer, A., Lammel, G., Kampf, C. J.: Aerosol Health Effects from
1479 Molecular to Global Scales, Environ. Sci. Technol. 51 (23), pp 13545–13567, 2017.

1480 Shrivastava, M., Cappa, C.D., Fan, J., et al: Recent advances in understanding secondary
1481 organic aerosol: Implications for global climate forcing, Rev. Geophys., 55, 509–559,
1482 doi:10.1002/2016RG000540, 2017.

1483 Spracklen, D. V., Jimenez, J. L., Carslaw, K. S., Worsnop, D. R., Evans, M. J., Mann, G.
1484 W., Zhang, Q., Canagaratna, M. R., Allan, J., Coe, H., McFiggans, G., Rap, A., and
1485 Forster, P.: Aerosol mass spectrometer constraint on the global secondary organic aerosol
1486 budget, Atmos. Chem. Phys., 11, 12109–12136, doi:10.5194/acp-11-12109-2011, 2011.

Tegen, I., Neubauer, D., Ferrachat, S., Siegenthaler-Le Drian, C., Bey, I., Schutgens, N., Stier, P., Watson-Parris, D., Stanelle, T., Schmidt, H., Rast, S., Kokkola, H., Schultz, M., Schroeder, S., Daskalakis, N., Barthel, S., Heinold, B., and Lohmann, U.: The global aerosol–climate model ECHAM6.3–HAM2.3 – Part 1: Aerosol evaluation, Geosci. Model Dev., 12, 1643-1677, https://doi.org/10.5194/gmd-12-1643-2019, 2019.

Thomson, D. S., Schein, M. E. and Murphy, D. M.: Particle Analysis by Laser Mass Spectrometry WB-57F Instrument Overview, Aerosol Sci. Technol., 33(1–2), 153–169, doi:10.1080/027868200410903, 2000.

Tilmes, S., Hodzic, A., Emmons, L.K., Mills, M.J., Gettelman, A., Kinnison, D.E., Park, M., Lamarque J.-F., Vitt, F., et al.: Climate forcing and trends of organic aerosols in the Community Earth System Model (CESM2), to be submitted to JAMES, 2019.

Tsigaridis, K., Daskalakis, N., Kanakidou, M., Adams, P. J., Artaxo, P., Bahadur, R., Balkanski, Y., Bauer, S. E., Bellouin, N., Benedetti, A., Bergman, T., Berntsen, T. K., Beukes, J. P., Bian, H., Carslaw, K. S., Chin, M., Curci, G., Diehl, T., Easter, R. C., Ghan, S. J., Gong, S. L., Hodzic, A., Hoyle, C. R., Iversen, T., Jathar, S., Jimenez, J. L., Kaiser, J. W., Kirkevåg, A., Koch, D., Kokkola, H., Lee, Y. H., Lin, G., Liu, X., Luo, G., Ma, X., Mann, G. W., Mihalopoulos, N., Morcrette, J.-J., Müller, J.-F., Myhre, G., Myriokefalitakis, S., Ng, N. L., O'Donnell, D., Penner, J. E., Pozzoli, L., Pringle, K. J., Russell, L. M., Schulz, M., Sciare, J., Seland, Ø., Shindell, D. T., Sillman, S., Skeie, R. B., Spracklen, D., Stavrakou, T., Steenrod, S. D., Takemura, T., Tiitta, P., Tilmes, S., Tost, H., van Noije, T., van Zyl, P. G., von Salzen, K., Yu, F., Wang, Z., Wang, Z., Zaveri, R. A., Zhang, H., Zhang, K., Zhang, Q., and Zhang, X.: The AeroCom evaluation and intercomparison of organic aerosol in global models, Atmos. Chem. Phys., 14, 10845–10895, doi:10.5194/acp-14-10845-2014, 2014.

Tsigaridis, K., and Kanakidou, M.: The Present and Future of Secondary Organic Aerosol Direct Forcing on Climate, Current Climate Change Reports, 2018, Volume 4, Issue 2, pp 84–98, 2018.

Turpin, B. J. and Lim, H. J.: Species contributions to PM2.5 mass concentrations: Revisiting common assumptions for estimating organic mass, Aerosol Sci. Tech., 35, 602–610, doi:10.1080/02786820152051454, 2001.

Ulbrich, I. M., Canagaratna, M. R., Zhang, Q., Worsnop, D. R. and Jimenez, J. L.: Interpretation of organic components from Positive Matrix Factorization of aerosol mass

spectrometric data, Atmos. Chem. Phys., 9(9), 2891–2918, doi:10.5194/acp-9-2891-2009, 2009.

van der Werf, G. R., Randerson, J. T., Giglio, L., Collatz, G. J., Mu, M., Kasibhatla, P. S., Morton, D. C., DeFries, R. S., Jin, Y., and van Leeuwen, T. T.: Global fire emissions and the contribution of deforestation, savanna, forest, agricultural, and peat fires (1997–2009), Atmos. Chem. Phys., 10, 11707-11735, https://doi.org/10.5194/acp-10-11707-2010, 2010.

Vergara-Temprado, J., Murray, B. J., Wilson, T. W., O'Sullivan, D., Browse, J., Pringle, K. J., Ardon-Dryer, K., Bertram, A. K., Burrows, S. M., Ceburnis, D., DeMott, P. J., Mason, R. H., O'Dowd, C. D., Rinaldi, M., and Carslaw, K. S.: Contribution of feldspar and marine organic aerosols to global ice nucleating particle concentrations, Atmos. Chem. Phys., 17, 3637-3658, https://doi.org/10.5194/acp-17-3637-2017, 2017.

Wang, J., Cubison, M. J., Aiken, A. C., Jimenez, J. L., and Collins, D. R.: The importance of aerosol mixing state and size-resolved composition on CCN concentration and the variation of the importance with atmospheric aging of aerosols, Atmos. Chem. Phys., 10, 7267-7283, https://doi.org/10.5194/acp-10-7267-2010, 2010.

Williamson, C. J., Kupc, A., Axisa, D., Bilsback, K.R., Bui, T., Campuzano-Jost, P., Dollner, M., Froyd, K., Hodshire, A. L., Jimenez, J. L., Kodros, J. K., Luo, G., Murphy, D. M., Nault, B. A., Ray, E. A., Weinzierl, B. B., Wilson, J. C., Yu, F., Yu, P., Pierce, J.F., Brock C. A.: A Large Source of Cloud Condensation Nuclei from New Particle Formation in the Tropics, Nature, 574, https://doi.org/10.1038/s41586-019-1638-9, 2019.

Wofsy, S.C., S. Afshar, H.M. Allen, E. Apel, E.C. Asher, B. Barletta, J. Bent, H. Bian, B.C. Biggs, D.R. Blake, N. Blake, I. Bourgeois, C.A. Brock, W.H. Brune, J.W. Budney, T.P. Bui, A. Butler, P. Campuzano-Jost, C.S. Chang, M. Chin, R. Commane, G. Correa, J.D. Crounse, P. D. Cullis, B.C. Daube, D.A. Day, J.M. Dean-Day, J.E. Dibb, J.P. DiGangi, G.S. Diskin, M. Dollner, J.W. Elkins, F. Erdesz, A.M. Fiore, C.M. Flynn, K. Froyd, D.W. Gesler, S.R. Hall, T.F. Hanisco, R.A. Hannun, A.J. Hills, E.J. Hintsa, A. Hoffman, R.S. Hornbrook, L.G. Huey, S. Hughes, J.L. Jimenez, B.J. Johnson, J.M. Katich, R.F. Keeling, M.J. Kim, A. Kupc, L.R. Lait, J.-F. Lamarque, J. Liu, K. McKain, R.J. Mclaughlin, S. Meinardi, D.O. Miller, S.A. Montzka, F.L. Moore, E.J. Morgan, D.M. Murphy, L.T. Murray, B.A. Nault, J.A. Neuman, P.A. Newman, J.M. Nicely, X. Pan, W. Paplawsky, J. Peischl, M.J. Prather, D.J. Price, E. Ray, J.M. Reeves, M. Richardson, A.W. Rollins, K.H. Rosenlof,

T.B. Ryerson, E. Scheuer, G.P. Schill, J.C. Schroder, J.P. Schwarz, J.M. St.Clair, S.D. Steenrod, B.B. Stephens, S.A. Strode, C. Sweeney, D. Tanner, A.P. Teng, A.B. Thames, C.R. Thompson, K. Ullmann, P.R. Veres, N. Vieznor, N.L. Wagner, A. Watt, R. Weber, B. Weinzierl, P. Wennberg, C.J. Williamson, J.C. Wilson, G.M. Wolfe, C.T. Woods, and L.H. Zeng. 2018. ATom: Merged Atmospheric Chemistry, Trace Gases, and Aerosols. ORNL DAAC, Oak Ridge, Tennessee, USA. https://doi.org/10.3334/ORNLDAAC/1581, 2018.

Woody, M. C., Baker, K. R., Hayes, P. L., Jimenez, J. L., Koo, B., and Pye, H. O. T.: Understanding sources of organic aerosol during CalNex-2010 using the CMAQ-VBS, Atmos. Chem. Phys., 16, 4081-4100, https://doi.org/10.5194/acp-16-4081-2016, 2016.

Yu, P., O. B. Toon, C. G. Bardeen, M. J. Mills, T. Fan, J. M. English, and R. R. Neely, Evaluations of tropospheric aerosol properties simulated by the community earth system model with a sectional aerosol microphysics scheme, J. Adv. Model. Earth Syst.,7, 865–914, doi:10.1002/2014MS000421, 2015.

Yu, P., Froyd, K. D., Portmann, R. W., Toon, O. B., Freitas, S. R., Bardeen, C. G., et al.: Efficient in-cloud removal of aerosols by deep convection. Geophysical Research Letters, 46. https://doi.org/10.1029/2018GL080544, 2019.

Zhang, K., O'Donnell, D., Kazil, J., Stier, P., Kinne, S., Lohmann, U., Ferrachat, S., Croft, B., Quaas, J., Wan, H., Rast, S., and Feichter, J.: The global aerosol-climate model ECHAM-HAM, version 2: sensitivity to improvements in process representations, Atmos. Chem. Phys., 12, 8911-8949, https://doi.org/10.5194/acp-12-8911-2012, 2012.

Zhang, Q. J., Beekmann, M., Drewnick, F., Freutel, F., Schneider, J., Crippa, M., Prevot, A. S. H., Baltensperger, U., Poulain, L., Wiedensohler, A., Sciare, J., Gros, V., Borbon, A., Colomb, A., Michoud, V., Doussin, J.-F., Denier van der Gon, H. A. C., Haeffelin, M., Dupont, J.-C., Siour, G., Petetin, H., Bessagnet, B., Pandis, S. N., Hodzic, A., Sanchez, O., Honoré, C., and Perrussel, O., 2013. Formation of organic aerosol in the Paris region during the MEGAPOLI summer campaign: evaluation of the volatility-basis-set approach within the CHIMERE model, Atmos. Chem. Phys., 13, 5767-5790, doi:10.5194/acp-13-5767-2013.

Zhang, X., Cappa, C. D., Jathar, S. H., McVay, R. C., Ensberg, J. J., Kleeman, M. J., and Seinfeld, J. H.: Influence of vapor wall loss in laboratory chambers on yields of secondary organic aerosol, P. Natl. Acad. Sci. USA, 111, 5802–5807, 2014.

1582 Zhao, G., Chen, Y., Hopke, P.K., Holsen, T.M., Dhaniyala, S.: Characteristics of traffic-
1583 induced fugitive dust from unpaved roads, Aerosol Science and Technology, 51:11, 1324-
1584 1331, DOI: 10.1080/02786826.2017.1347251, 2017.

1585 Zhu, J., Penner, J. E., Yu, F., Sillman, S., Andreae, M., and Coe, H.: Organic aerosol
1586 nucleation, climate and land use change: Decrease in radiative forcing, Nature
1587 Communications, 10, Article No. 423, https://www.nature.com/articles/s41467-019-
1588 08407-7, 2019.

1589 Zotter, P., I. El-Haddad, Y. Zhang, P.L. Hayes, X. Zhang, Y.H. Lin, L. Wacker, J. Schnelle-
1590 Kreis, G. Abbaszade, R. Zimmermann, J.D. Surratt, R. Weber, J.L. Jimenez, S. Szidat, U.
1591 Baltensperger, A.S.H. Prévôt. Diurnal cycle of fossil and non-fossil carbon using
1592 radiocarbon analyses during CalNex. Journal of Geophysical Research-Atmospheres,
1593 119, 6818–6835, doi:10.1002/2013JD021114, 2014.

1594

1595 Tables

1596 Table 1: ATom global model configurations and their treatment of the most important processes affecting organic aerosols.

Models & horizontal res. & met. fields & config. reference	**Aerosol module**	**Submicron size[6] OA (dust/sea salt)**	**SOA precursors[1]**					**SOA production**	**Emission**	**POA/POC (SOA/SOC)**	**Removal**		
			ISO	**MT**	**SQ**	**ANT**	**$C_{>12}$**				**Standard[2]**	**Improved**	**Photolytic**
CESM1-CARMA (1.9°lon x 2.5°lat) MERRA-2 (Yu et al. 2019)	20 bins	< 500 nm (< 800 nm)	x	x		x		Semi-volatile using VBS (Pye et al. 2010)	GAIS and GFED v3	1.8 (N/A)	x	For convective updrafts (Yu et al. 2019)[3]	
CESM2-DYN (0.9° lon x 1.25° lat) GEOS5 (Tilmes et al. 2019)	4 modes	< 270 nm (< 800 nm)	x	x	x	x	x	Semi-volatile using VBS (Hodzic et al. 2016)	CMIP6 and QFED v2.4	1.8 (N/A)	x	Water solubility of organic gases per Hodzic et al. (2014)	For SOA (Hodzic et al. 2016)
CESM2-SMP GEOS5 (0.9° lon x 1.25° lat) (Tilmes et al. 2019)	4 modes	< 270 nm (< 800 nm)	x	x		x		Non-volatile with prescribed mass yields for all precursors[4]	CMIP6 and QFED v2.4	1.8 (N/A)	x		
ECHAM6-HAM ECHAM6 (1.87°lon x1.87°lat) (Tegen et al. 2019)	7 modes	< 500 nm (< 500 nm)		x				Non-volatile with 15% prescribed mass yields (Dentener et al. 2006)	ECLIPSE[5] and GFAS	1.4 (1.4)	x		
GC12-REF (2° lon x 2.5° lat) GEOS-FP (Bey et al. 2001)	Bulk	Bulk (< 500 nm)	x	x	x	x		Semi-volatile using VBS (Pye et al. 2010); non-volatile isoprene-	CMIP6 and GFED v4	2.1 (N/A)	x	For convective updrafts per Wang et al. 2014	

								SOA (Marais et al. 2016)					
GC12-DYN (2° lon x 2.5° lat) GEOS-FP (Bey et al. 2001)	Bulk	Bulk (< 500 nm)	x	x	x	x	x	Semi-volatile using VBS (Hodzic et al. 2016); non-volatile isoprene-SOA (Marais et al. 2016)	CMIP6 and GFED v4	2.1 (N/A)	x	For convective updrafts (Wang et al. 2014); Water solubility of organic gases (Hodzic et al. 2014)	For SOA (Hodzic et al. 2016)
GC10-TOMAS (5° lon x 4° lat) GEOS-FP (Kodros et al. 2016)	15 bins	< 316 nm (< 316 nm)		x		x		Non-Volatile using 10% mass yields for MT, 0.2 Tg SOA per Tg CO for anthropogenic emissions	EDGAR v4 and GFED v3	1.8 (1.8)	x	For convective updrafts (Wang et al. 2014)	
GEOS5 (0.5°lon x 0.625°lat) MERRA-2 (Bian et al. 2019)	Bulk	bulk (< 1 μm for dust, 500 nm for seasalt)	x	x		x		Non-Volatile, 10% mass yields for all precursors	HTAP and QFED v2.54	1.8 (1.8)	x		

(1) SOA precursors include isoprene (ISO), monoterpenes (MT), sesquiterpenes (SQ), anthropogenics (ANT) including aromatics such as benzene, toluene and xylene, as well as lumped shorter chain alkanes and alkenes; and higher molecular weight n-alkanes and n-alkenes (C>12).

(2) Standard removal includes dry deposition and sedimentation, as well as convective and large-scale scavenging of soluble organic gases and aerosols, and below-cloud scavenging of aerosols.

(3) A sensitivity simulation is performed with CESM1-CARMA without the improved scavenging in convective updrafts.

(4) 5% for lumped C<12 alkanes, 5% for lumped C<12 alkenes, 15% for aromatics, 4% for isoprene, 25% for monoterpenes.

(5) Anthropogenic BC emission are replaced in Russia with the dataset of Huang et al. (2015).

(6) Submicron size range (diameter) used in various models for comparison with the AMS data.

Table 2: Comparison of observed and simulated OA concentrations along ATom-1 and ATom-2 flights for eight global model simulations and their ensemble. The results of the model ensemble are also indicated. The statistical indicators are calculated as normalized mean bias $NMB(\%) = 100 \times \sum_i (M_i - O_i) / \sum_i O_i$; normalized mean error $NME(\%) = 100 \times \sum_i |(M_i - O_i)| / \sum_i O_i$; root mean square error $RMSE(\mu g\ m^{-3}) = \sqrt{(1/N) \sum_i (M_i - O_i)^2}$ and correlation coefficient (R^2) between modeled (M_i) and observed (O_i) data points. The mean of ATom-1 observations is ~0.23 μg m^{-3} and for ATom-2 is 0.11 μg m^{-3}. Figure S4 shows the normalized mean bias for all individual ATom model simulations for various latitudinal regions and for both the Atlantic and Pacific basins.

Organic aerosols	Avg.Mod. (μg m^{-3})	NMB (%)	NME (%)	RMSE (μg m^{-3})	R^2	Avg.Mod. (μg m^{-3})	NMB (%)	NME (%)	RMSE (μg m^{-3})	R^2
Model	*ATom-1 scores (August 2016)*					*ATom-2 scores (February 2017)*				
AeroCom-II Ens.	0.400	74.2	127.3	0.560	0.31	0.254	137	175	0.278	0.38
AeroCom-II Sub.(1)	0.335	47.0	111	0.557	0.28	0.242	127	178	0.290	0.27
ATom Ensemble	0.239	-4.5	64.6	0.372	0.66	0.139	23	92.6	0.224	0.48
CESM2-DYN	0.268	4.6	83.7	0.867	0.47	0.140	25.6	111.7	0.317	0.36
CESM2-SMP	0.349	36.3	94.3	0.556	0.51	0.175	57.2	125.4	0.299	0.31
CESM1-CARMA	0.155	-33.2	93.8	0.603	0.12	0.131	22.6	119.6	0.244	0.31
ECHAM6-HAM	0.400	73.6	143.6	0.714	0.24	0.214	100	184.0	0.363	0.23
GC12-DYN	0.142	-32.6	79.4	0.560	0.16	0.174	14.7	96.6	0.312	0.39
GC12-REF	0.122	-43.0	76.5	0.536	0.18	0.147	3.6	96.3	0.292	0.35
GC10-TOMAS	0.218	-14.4	86.5	0.644	0.16	0.313	150.0	223.7	0.537	0.12
GEOS5	0.242	-5.4	86.6	0.975	0.38	0.084	-24.9	86.4	0.268	0.29

(1) This is the subset of AeroCom-II model ensemble that includes only seven models that are similar to those that are included in the ATom ensemble (either the same model, or an older model version, or the same aerosol module). AeroCom-II Sub. incudes CAM5-MAM3, CCSM4-hem, ECHAM5-HAM2,

GEOSChem-APM 8.2, GEOSChem 9, GISS-TOMAS and GMI (see Tsigaridis et al., 2014 for their description).

Figures:

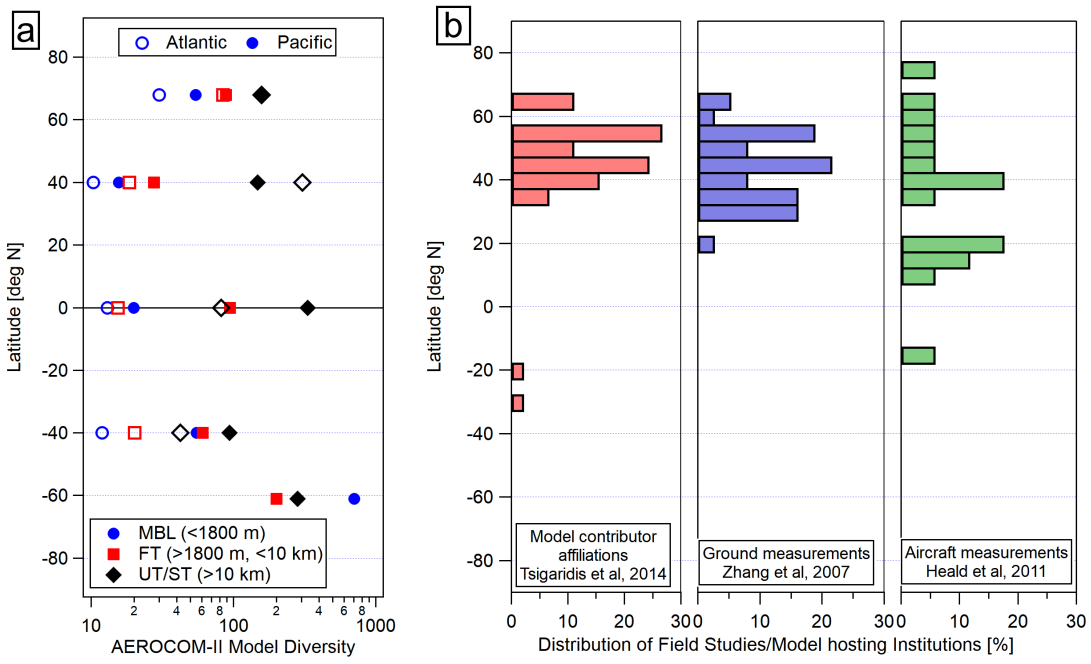

Figure 1: (a, left) The ratio between the average OA concentrations of the highest and the lowest models (for each region) as predicted among 28 global chemistry transport models participating in the AeroCom phase II intercomparison study (Tsigaridis et al. 2014); (b, right) Geographical distribution of institutions at which the AeroCom-II models were ran/developed (based on author affiliations) and of the field measurements included in two major literature overview studies (Zhang et al., 2007; Heald et al., 2011) for the OA ground and aircraft AMS as a function of latitude. For the aircraft campaigns, the average latitude for the full deployment was taken.

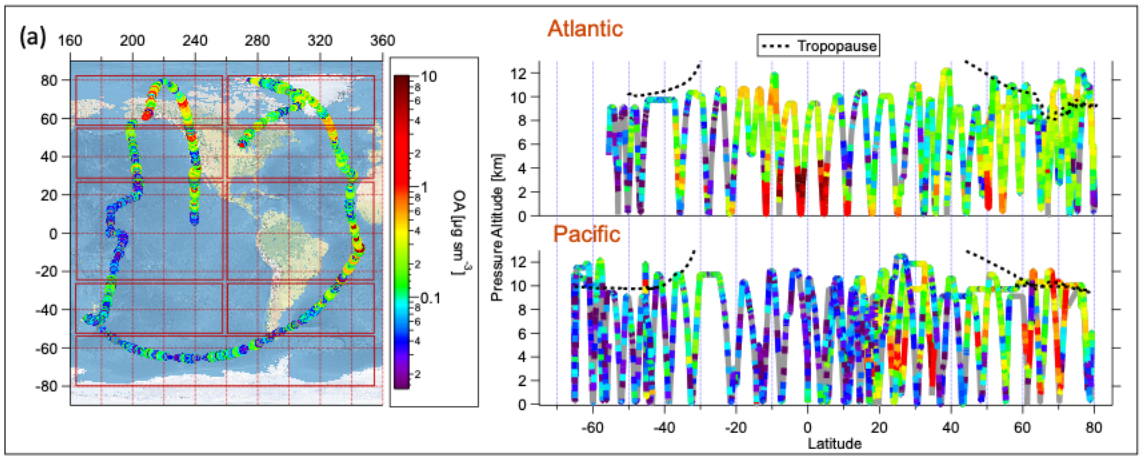
(a)
Atlantic
Tropopause
Pacific
Pressure Altitude [km]
Latitude
OA [μg sm-3]

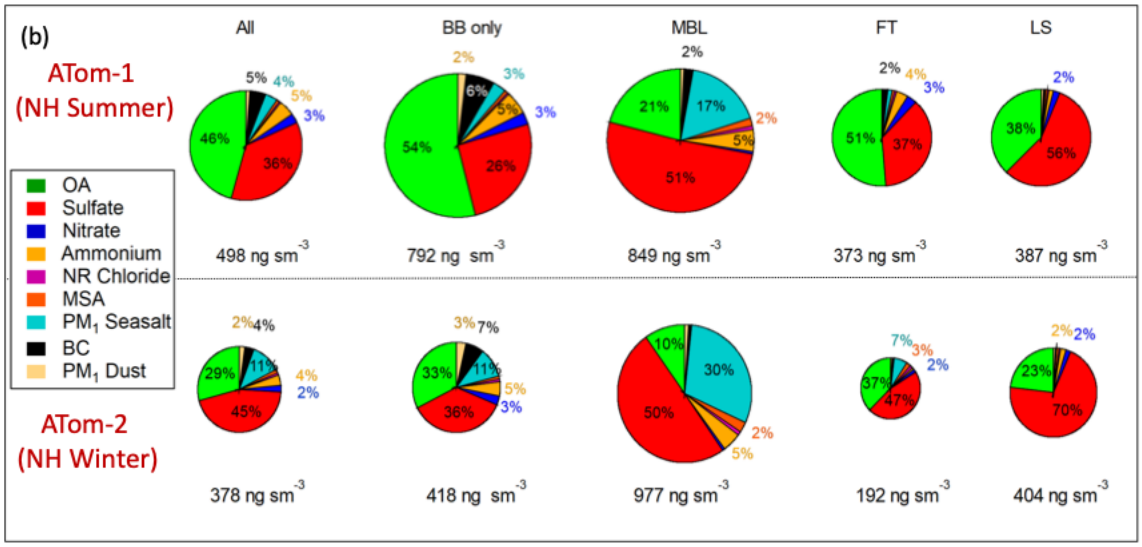
(b)
ATom-1
(NH Summer)
ATom-2
(NH Winter)
OA
Sulfate
Nitrate
Ammonium
NR Chloride
MSA
PM1 Seasalt
BC
PM1 Dust
All
BB only
MBL
FT
LS
498 ng sm-3
792 ng sm-3
849 ng sm-3
373 ng sm-3
387 ng sm-3
378 ng sm-3
418 ng sm-3
977 ng sm-3
192 ng sm-3
404 ng sm-3

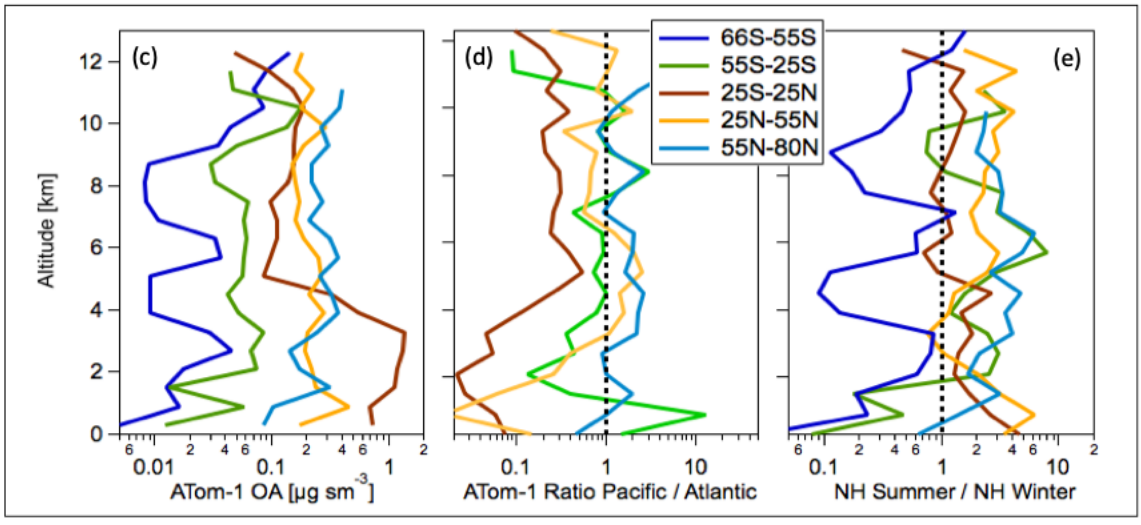
(c)
(d)
(e)
66S-55S
55S-25S
25S-25N
25N-55N
55N-80N
Altitude [km]
ATom-1 OA [μg sm-3]
ATom-1 Ratio Pacific / Atlantic
NH Summer / NH Winter

1636

Figure 2: (a, left) ATom-1 DC-8 flights during the August 2016 deployment. Red boxes indicate regions used for the latitude averaging of the model results. (a, right) Vertical distribution of OA concentrations (μg sm^{-3}) along ATom-1 flight tracks (b) Average submicron aerosol composition as measured in the biomass-burning influenced regions (BB only), and the non-BB influenced regions including the marine boundary layer (MBL), free troposphere (FT), and lower stratosphere (LS) for ATom-1 (upper plots) and ATom-2 (lower plots). The BB influenced airmasses were filtered using the PALMS data (see section 3.1). Contributions below 2% are shown but not labeled on the pie chart graph. In ATom-1, BB-only represents 24% of the data, clean MBL 8%, clean FT 57% and clean UT 12%, whereas in ATom-2 BB-only represents 3%, clean MBL 8%, clean FT 74%, clean UT 16%. (c) The average OA vertical profiles are shown for each latitude region as well as (d) the ratios between the Pacific and Atlantic Oceans in each region. (e) The seasonal contrast in OA concentrations as calculated as the ratio in OA concentrations between the NH summer (ATom-1) and NH winter (ATom-2) campaigns. The corresponding plots for ATom-2 can be found in Fig. S1.

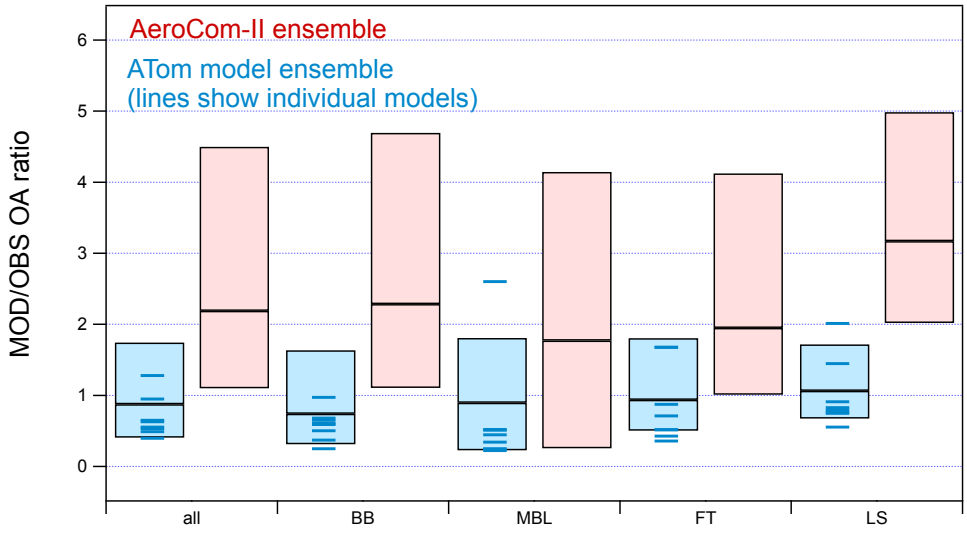

Figure 3: Ratios between predicted and observed OA concentrations for all ATom-1 flights as calculated for the ATom and AeroCom-II model ensembles in different regions ("BB" biomass burning influenced regions; "MBL" clean marine boundary layer; "FT" clean free troposphere' and "LS" lower stratosphere). Median of the ensemble ratio is shown as a horizontal line, while the boxes indicate 25th and 75th percentiles. Medians for the individual models included in the current ATom model ensemble are also shown as blue lines.

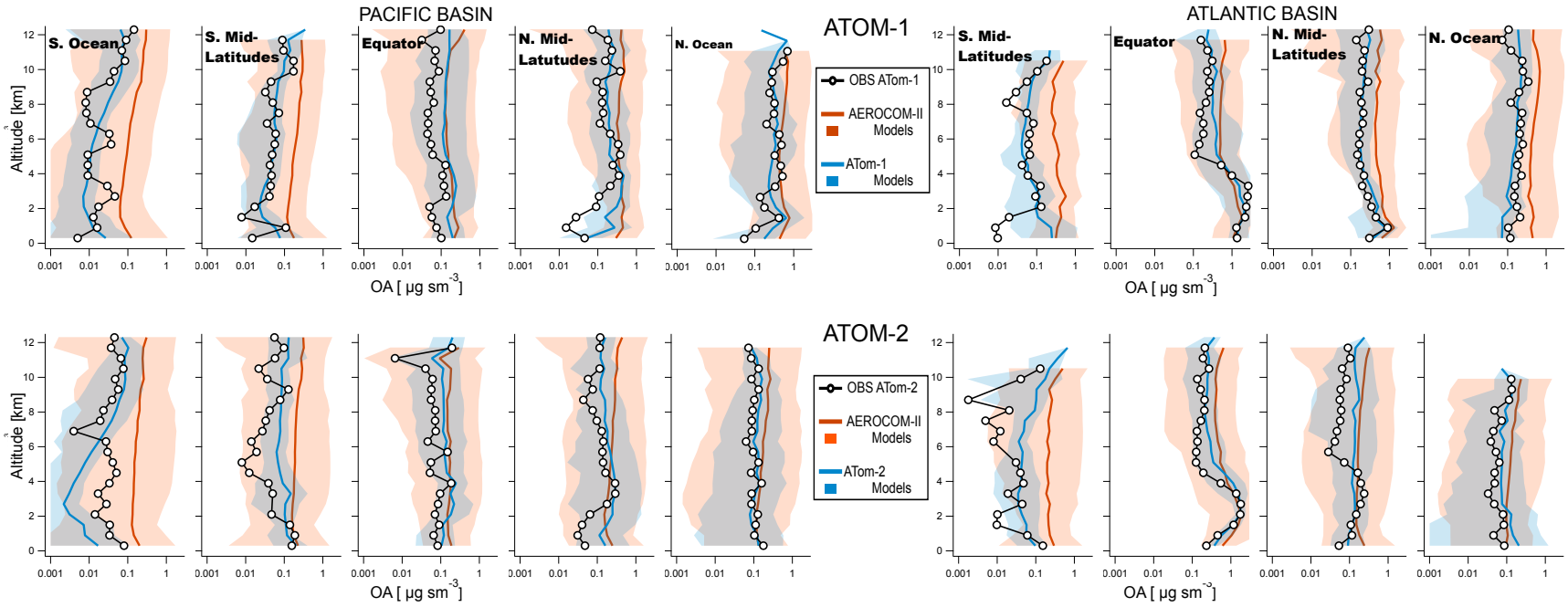

1660

1661

1662 Figure 4: Comparison of latitude-averaged predicted OA vertical profiles with ATom-1 and -2 measurements taken over the Pacific (left
1663 side) and Atlantic (right side) basins. Results of the AeroCom-II model ensemble average are shown in red while those of the ATom
1664 model ensemble are shown in blue. Shaded areas indicate the variability (two standard deviations) within each model ensemble.

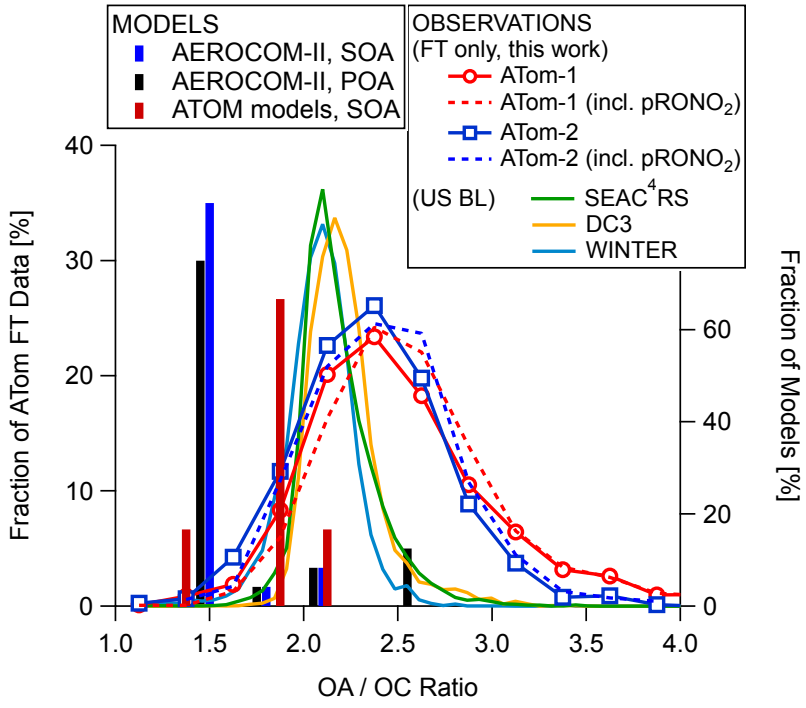

Figure 5: Distribution of the OA / OC ratio as measured during ATom-1 and -2. Values for the recent aircraft campaigns (SEAC4RS, DC3 and WINTER) that took place over continental US regions closer to continental source regions are also shown (Schroder et al., 2018). The bars (right axis) show the OA/OC used for SOA and POA by the models included in the AeroCom and ATom ensemble, with OA/OC=1.4 being the modal value for the former and 1.8 for the latter.

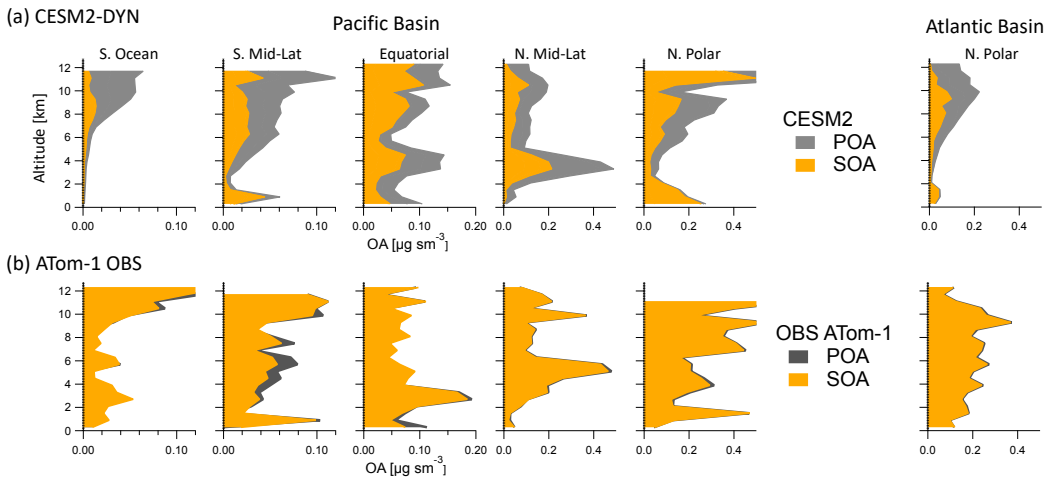

1673

1674 Figure 6: Comparison of averaged POA and SOA vertical profiles as observed during
1675 ATom and as predicted by the CESM2-DYN model over the non-BB influenced Pacific
1676 and Atlantic basins. The comparison is not shown for the strongly biomass burning
1677 influenced regions as all the OA is conservatively allocated to POA in those regions.

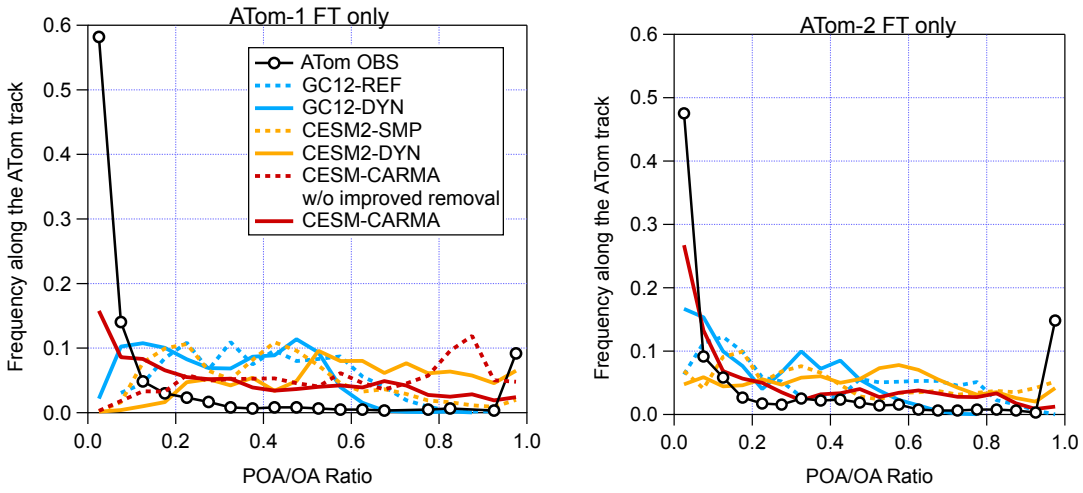

1678

1679 Figure 7: Frequency distribution of observed and simulated ratio of POA to total OA in the
1680 free troposphere during ATom-1 and ATom-2 as computed by the GC12-, CESM2-, and
1681 CESM1-CARMA models.

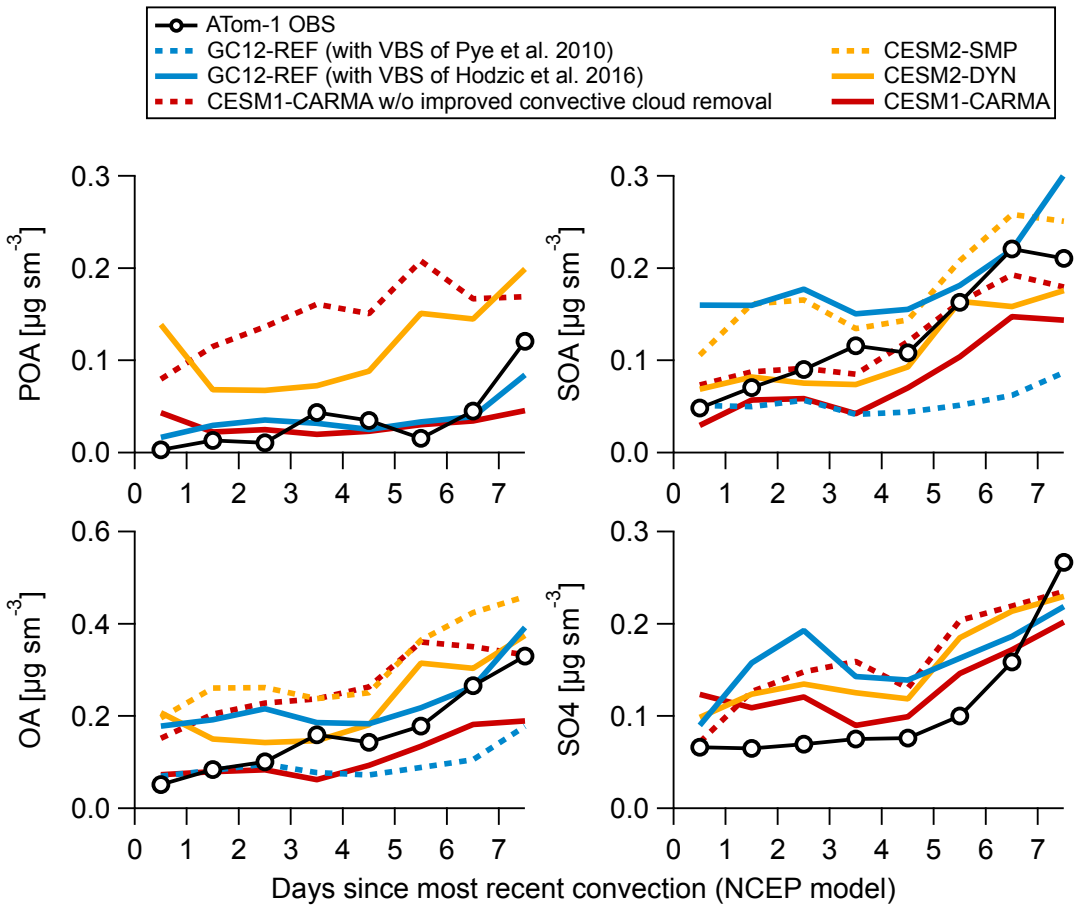

1682

1683 Figure 8: Measured and predicted mass concentrations of POA, SOA, OA and sulfate
1684 aerosols during ATom-1 as a function of the number of days since the air mass was
1685 processed through convection (based on a trajectory model from Bowman, 1993, and
1686 satellite cloud data from NASA Langley, https://clouds.larc.nasa.gov/). CESM2-SMP and
1687 CESM2-DYN have the same emissions and processing of POA and sulfate, and thus
1688 similar concentrations. The same is true for the two versions of GC12.

1689

1690

1691

(a)

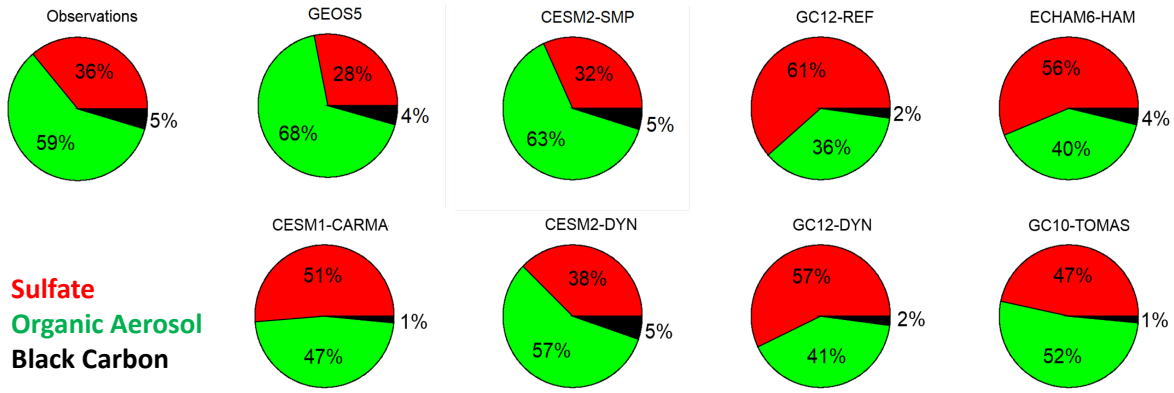

(b)

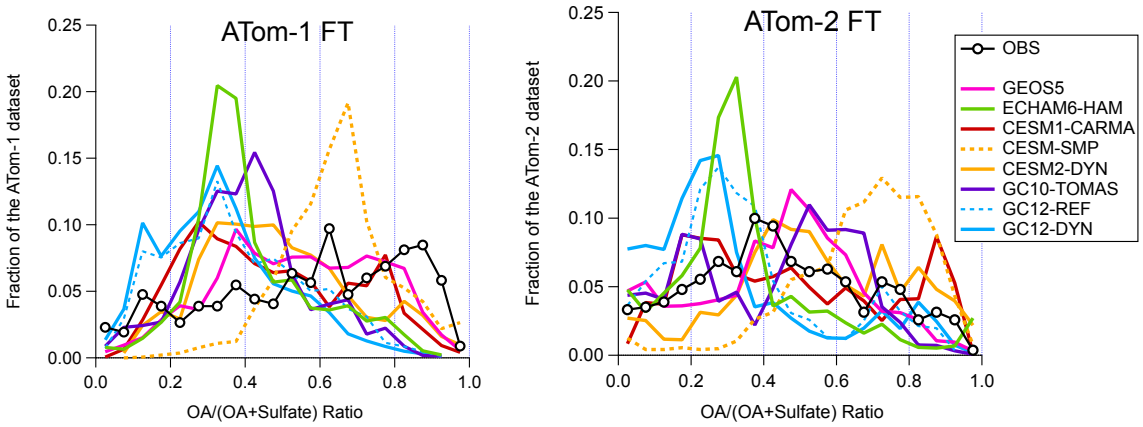

Figure 9: (a) Predicted and measured composition of submicron aerosols in the free troposphere as a function of the submicron aerosol mass concentrations during ATom-1. (b) Frequency distribution of observed and simulated ratio of organic to organic plus sulfate aerosols in the free troposphere during ATom-1 and -2.

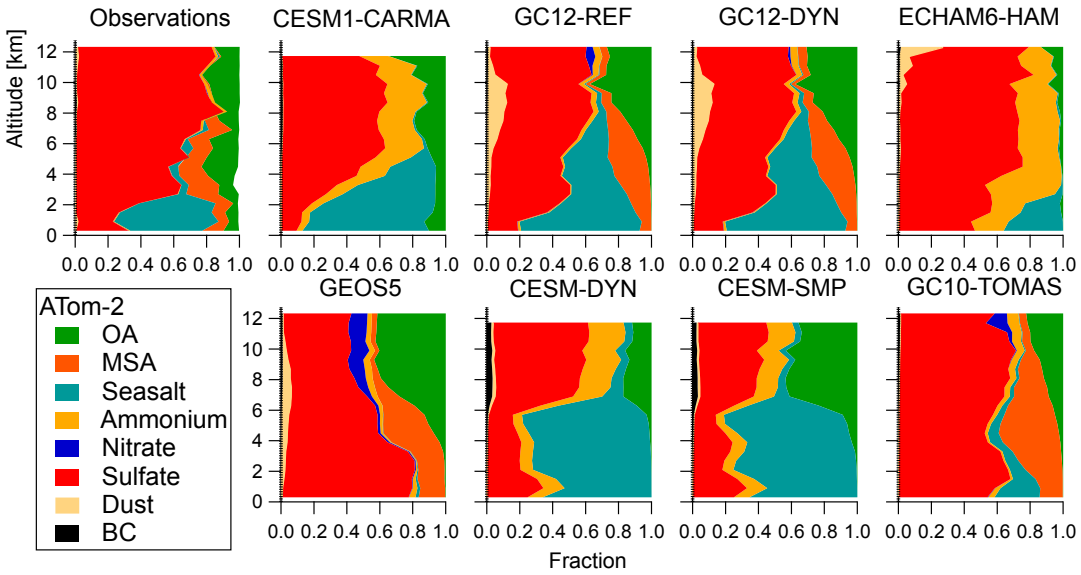

Figure 10: Comparison of measured and predicted composition of submicron aerosols as a function of altitude over the remote Southern Ocean region during NH Winter (ATom-2). For models that do not calculate ammonium in the aerosol (such as CESM1-CARMA, CESM2-SMP, CESM2-DYN and ECHAM6-HAM), ammonium was estimated from the sulfate mass assuming the formation of ammonium sulfate. Note that while the modeled and measured submicron sea salt size ranges agree fairly well (Table 1), this is not quite the case for dust. Given that the accumulation mode dust in the models presented contains larger sizes than the AMS range (< 500 nm), it is expected for the modeled dust concentration to be larger than measured.

1713